

Exploration of Novel Therapeutic Benzoxazines as Anti-Breast Cancer Agents: DFT Computations and In Silico Predictions

Karthik Nallasamy¹ , Sumathi Sivaraman¹ , Jeyavijayan Subbiah^{1,*} 

¹ Department of Physics, Kalasalingam Academy of Research and Education (Deemed to be University), Krishnankoil 626 126, India; 9923126007@klu.ac.in (K.N.); 9923126012@klu.ac.in (S.S.);

* Correspondence: s.jeyavijayan@klu.ac.in(J.S);

Received: 24.10.2024; Accepted: 15.07.2025; Published: 30.09.2025

Abstract: The present investigation deals with the structural and pharmacokinetic properties of 2-phenyl-4H-3,1-benzoxazin-4-one and 2-(4-fluorophenyl)-4H-3,1-benzoxazin-4-one. In this study, optimized structures of molecules have been determined using the Gaussian 09 program with density functional theory (DFT) and B3LYP/6-311++G(d,p) basis set. In addition, thermodynamic parameters, Mulliken charges, UV-Vis, HOMO-LUMO, DOS, and Natural population analysis of molecules have been performed. The interaction between bonding and anti-bonding orbitals and their stabilisation energies was computed using the NBO technique. The molecular electrostatic potential (MEP) energy surface has been used to study the most reactive areas of the molecules. The Hirshfeld surfaces and fingerprint techniques have been used to study the inter- and intramolecular interactions of the molecules. Topological research, including thermodynamic parameters, LOL, and ELF, has been carried out. From the docking analysis, the breast cancer inhibitors showed the highest binding affinity of -10.4 and -10.6 kcal/mol for both molecules, which are comparable with the binding affinity of the breast cancer standard drug anastrozole. Finally, ADMET profiles of the molecules have been found to indicate their toxicity and drug-likeness.

Keywords: benzoxazine; breast cancer; density functional theory; molecular docking; ADMET.

© 2025 by the authors. This article is an open-access article distributed under the terms and conditions of the Creative Commons Attribution (CC BY) license (<https://creativecommons.org/licenses/by/4.0/>), which permits unrestricted use, distribution, and reproduction in any medium, provided the original work is properly cited. The authors retain copyright of their work, and no permission is required from the authors or the publisher to reuse or distribute this article, as long as proper attribution is given to the original source.

1. Introduction

Cancer is a complex group of diseases characterized by the uncontrolled growth and spread of abnormal cells in the body. There are more than 100 different types of cancer, each with its own unique features and behaviours [1]. The exact cause of cancer is often not fully understood, but it usually involves a combination of genetic, environmental, and lifestyle factors. Some common risk factors for cancer include tobacco use, excessive alcohol consumption, unhealthy diet, lack of physical activity, exposure to certain chemicals and radiation, as well as genetic predisposition [2]. Common treatment options include surgery, chemotherapy, radiation therapy, immunotherapy, targeted therapy, hormone therapy, and stem cell transplantation. Breast cancer is the most common type of cancer among women worldwide, and the ICMR estimated that around 1.4 lakh new cases of breast cancer were diagnosed in India [3], with the age group of persons suffering ranging from 20 to 60 years of age [4]. Research has been done on the potential use of benzoxazin derivatives in the treatment

and investigation of breast cancer [5,6]. In cases of breast cancer, benzoxazine compounds show promise as anticancer agents. These substances can suppress cell growth and inhibit oncogenic signalling pathways associated with breast cancer progression.

Hence, benzoxazine derivatives such as 2-phenyl-4H-3,1-benzoxazine-4-one (2PB) and 2-(4-fluorophenyl)-4H-3,1-benzoxazine-4-one (2FPB) have been selected in this study. Further, according to a thorough study of the literature, 2FPB has not yet been subjected to deep theoretical investigation, although 2PB has already been published [7], but not in detail. The 2PB molecule has a phenyl group (C₆H₅) attached to the carbon atom at position 2 of the benzoxazine ring. In the 2FPB molecule, the 4-fluorophenyl group (C₆H₄F) is attached to the carbon atom at position 2 of the benzoxazine ring. The Lee Yang and Parr (LYP) connection functional, which recovers the energetic electron link, and Becke's 3-parameter (B3) exchange-correlation are the most effective DFT calculations. A detailed Hirshfeld surface investigation using a 2D finger plot was conducted for selected molecules to understand the numerous interpolating interactions. In addition, calculations using DFT have been used to establish several molecular features through Mullikan population, DOS spectrum, MEP plot, (HOMO-LUMO) analysis, and natural population analysis. In addition, the thermodynamic properties and polarity of the molecules have been studied. ELF and LOL studies have been performed, and RDG was used to study weak interactions to determine the binding nature of the molecules. To verify their anti-breast cancer effect, docking experiments on the aforementioned molecules have been performed on proteins linked to breast cancer, and ADMET analysis has been revealed for their drug-likeness.

2. Materials and Methods

2.1. Quantum chemical calculations.

DFT calculations have been carried out using the Gaussian 09W [8] molecular software program using the DFT/B3LYP/6-311++G (d,p) method. A time-dependent (TD)-DFT/B3LYP approach has been used to study the UV-Vis spectra [9]. Prediction of Frontier molecular orbitals (FMO) and MEP of selected molecules and identification of their optimal structure was done using Gauss View 05 software [10]. Since intermolecular delocalizations quantify the second-order interactions between the empty orbitals of one subsystem and the full orbitals of another subsystem, NBO computations have been performed. Apart from these computations, TDOS spectra in the molecules have been generated using the GaussSum [11]. Natural population and Mulliken analysis have been used to study the electron distribution in different atomic orbital subshells at the theoretical level. The topological qualities have been evaluated, and the ELF, LOL, and RDG plots have been generated using the Multiwfn programme [12].

2.2. Hirshfeld surface analysis.

The CIF files of molecules have been utilised to calculate brief interactions between neighbouring molecules using Crystal Explorer 3.0 [13]. It was intended to visualise the interaction energies and the two-dimensional (2D) fingerprint plot of brief interatomic encounters. The parameters obtained from the normalised contact distance d_{norm} have been represented by a colour gradient, ranging from red to blue, and have been expressed in terms of the atoms' van der Waals radii (vdW), d_i , and d_e parameters [14]. The parameters used to 2D fingerprint plots between d_i and d_e show the distances of the Hirshfeld surface from the

nearby atomic centres. The collection of interactions was determined using 2D finger plots between di and de within the region of 1.0-2.4 Å. The light red areas signify poor interactions, the blue spots represent non-interacting regions, and the deep red spots reflect short interatomic contacts. Hirshfeld surface shape-index is a method to visualise stacking interactions between π and π . The planar stacking of molecules is characterised by vast, comparatively flat patches on the curved surfaces. Moreover, distinguishing characteristics may be found on the shape index plots, which are useful for examining how different molecules pack against one another.

2.3. Molecular docking analysis.

After DFT calculations, the compounds under investigation were then used for molecular docking. Proteins associated with breast cancer have been retrieved from the RCSB PDB data bank under PDB IDs 1AQU and 1M17 [15]. In addition, conventional anastrozole drugs have been tested for docking with these two proteins [16]. The PyRx 0.8 Auto Dock Vina program [17] has been used to conduct docking investigations, and BIOVIA Discovery Studio Visualizer [18] was used to display docking results. Before molecular docking, hydrogens are added, the chain is free of active sites, and water molecules and ligands are removed from the protein structures. After energy minimization, the targeted proteins were saved as macromolecules in the “.pdbqt” format, and the selected molecules were saved in this format. The grid box was positioned in the active site, and molecular docking was performed using the AutoDock query method in PyRx 0.8 following the import of the targeted proteins and ligand molecules. Docking is used to calculate the binding values of ligands and proteins. BIOVIA Discovery Studio was used to visualize PyRx output files. The data have been analysed to identify interacting bonds, amino acid residues, and bond lengths. The Discovery Studio Visualizer program was used to visualize the protein-ligand complex. 2D and 3D drawings have been produced, and the interactions between the ligands and target proteins have been characterised.

2.4. Pharmacokinetic studies.

The pharmacokinetic and physicochemical characteristics of the medicinal molecules have been determined using the pkCSM server. The SMILES of the molecules have been obtained from the PubChem database and loaded into the pkCSM server in order to determine the physicochemical and pharmacokinetic properties, such as absorption, aqueous solubility, distribution, metabolism, excretion, and toxicity, based on the chemical structure of the molecules [19]. The BOILED-Egg model was then run using the Swiss-ADME web server, and a number of pharmacokinetic properties, including drug similarity, lipophilicity, water solubility, and a radar plot, were predicted.

3. Results and Discussion

3.1. Molecular structure analysis.

Figure 1 shows molecular structures of 2PB and 2FPB. The optimal global minimum energy for 2PB and 2FPB is determined to be -744.328934 and -843.597776 Hartrees, respectively. The calculated bond lengths C2-C16, O3-C4, C6-C15, and C13-C15 are 1.474, 1.401, 1.410, 1.405 Å for 2PB and 1.472, 1.403, 1.411 and 1.404 Å for 2FPB, which have C1 point group and these values are compared with experimental XRD values [20] of 1.462, 1.379,

1.393 and 1.394 Å as shown in Table 1. It is found that these bond lengths somewhat deviate from the experimental data because the theoretical calculations are related to isolated molecules in the gaseous phase, whereas the experimental data are related to solid-state molecules. Since C4 is bonded to two oxygen atoms (O3 and O5), the expanded bond length of C4-C6 (1.461 Å by B3LYP and 1.448 Å by experimental) offers a clear comprehension of the impact of the ring structure. This demonstrates unequivocally that the π -electrons surrounding the C4-C6 bond are not delocalized. Table 1 also shows that the C-C bonds have a larger force of attraction between carbon and carbon, making them stronger than C-H bonds, with bond lengths ranging from 1.082 to 1.084 Å. Compared to other C-C-C angles, the computed bond angle of the C16-C17-C19 is larger at 122.6° in both molecules (122.9° by experiment), since bond angles increase with increasing atom electronegativity. According to the observed values of 118.7°, 119.2°, and 122.9° for the oxygen and nitrogen atom assembly coupled at C4 and C2, the computed angles between C4-C6-C15, C2-C16-C17, and N1-C2-C16 are 118.8°, 119.3°, and 122.6°, respectively, in both molecules. The electronegativity of the oxygen and nitrogen atoms, O3, O5, and N1, is the cause of these asymmetries. Furthermore, an illustration of the regression correlation graph is shown for the experimental and computed parameters of the molecules. For 2PB, $R^2 = 0.9879$ (bond length), 0.9238 (bond angle), and for 2FPB, $R^2 = 0.8717$ (bond length), 0.9019 (bond angle), as shown in Figure 2, respectively.

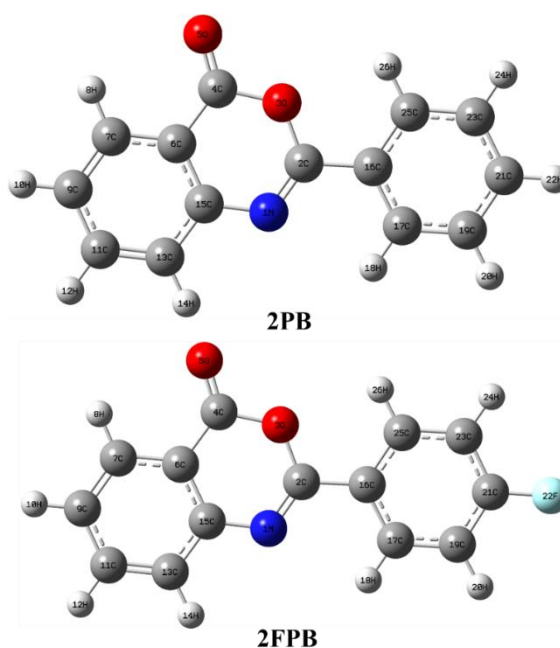


Figure 1. Optimized structures of 2-phenyl-4H-3,1-benzoxazin-4-one and 2-(4-fluorophenyl)-4H-3,1-benzoxazin-4-one.

Table 1. The optimized structural parameters of 2-phenyl-4H-3,1-benzoxazin-4-one and 2-(4-fluorophenyl)-4H-3,1-benzoxazin-4-one.

Bond length (Å)	DFT-B3LYP/6-311++G(d,p)		Experimental ^[20]
	2PB $R^2=0.9879$	2FPB $R^2=0.8717$	
N1-C2	1.283	1.283	1.275
N1-C15	1.386	1.386	1.394
C2-O3	1.368	1.367	1.370
C2-C16	1.474	1.472	1.462
O3-C4	1.401	1.403	1.379
C4-O5	1.199	1.199	1.193
C4-C6	1.461	1.461	1.448
C6-C7	1.401	1.401	1.387

Bond length (Å)	DFT-B3LYP/6-311++G(d,p)		Experimental ^[20]
	2PB R ² = 0.9879	2FPB R ² = 0.8717	
C6-C15	1.410	1.411	1.393
C7-H8	1.083	1.083	0.930
C7-C9	1.385	1.385	1.371
C9-H10	1.083	1.083	0.930
C9-C11	1.404	1.404	1.381
C11-H12	1.084	1.084	0.930
C11-C13	1.386	1.386	1.369
C13-H14	1.083	1.083	0.930
C13-C15	1.405	1.404	1.394
C16-C17	1.403	1.403	1.384
C16-C25	1.402	1.402	1.388
C17-H18	1.082	1.082	0.930
C17-C19	1.389	1.388	1.371
C19-H20	1.084	1.083	0.930
C19-C21	1.396	1.389	1.374
C21-H22 (F22)	1.084	1.352	0.930
C21-C23	1.394	1.386	1.367
C23-H24	1.084	1.083	0.930
C23-C25	1.392	1.391	1.376
C25-H26	1.082	1.082	0.930
Bond angle (°)	R²= 0.9238	R²= 0.9019	
C2-N1-C15	118.3	118.2	117.8
N1-C2-O3	124.5	124.6	124.7
N1-C2-C16	122.6	122.6	122.9
O3-C2-C16	112.9	112.8	112.4
C2-O3-C4	122.3	122.3	121.6
O3-C4-O5	117.8	117.7	117.0
O3-C4-C6	114.3	114.2	115.3
O5-C4-C6	128.0	128.1	127.7
C4-C6-C7	120.5	120.5	120.7
C4-C6-C15	118.8	118.8	118.7
C7-C6-C7	120.7	120.7	120.6
C6-C7-H8	118.8	118.8	120.2
C6-C7-C9	119.7	119.7	119.6
H8-C7-C9	121.5	121.5	120.0
C7-C9-H10	120.1	120.1	120.0
C7-C9-C11	119.9	119.9	120.0
H10-C9-C11	120.0	120.0	120.0
C9-C11-H12	119.6	119.6	120.0
C9-C11-C13	120.9	120.9	121.3
H12-C11-C13	119.5	119.5	120.3
C11-C13-H14	121.6	121.6	120.3
C11-C13-C15	120.0	120.0	119.5
H14-C13-C15	118.4	118.5	120.3
N1-C15-C6	121.8	121.8	121.7
N1-C15-C13	119.3	119.3	119.2
C6-C15-C13	118.9	118.9	119.1
C2-C16-C17	119.3	119.3	119.2
C2-C16-C25	121.2	121.3	121.6
C17-C16-C25	118.3	118.2	117.8
C16-C17-H18	124.5	124.6	124.7
C16-C17-C19	122.6	122.6	122.9
H18-C17-C19	112.9	112.8	112.4
C17-C19-H20	122.3	122.3	121.6
C17-C19-C21	117.8	117.7	117.0
H20-C19-C21	114.3	114.2	115.3
C19-C21-H22 (F22)	128.0	128.1	127.7

Bond length (Å)	DFT-B3LYP/6-311++G(d,p)		Experimental ^[20]
	2PB R ² = 0.9879	2FPB R ² = 0.8717	
C19-C21-C23	120.5	120.5	120.7
(F22) H22-C21-C23	118.8	118.8	118.7
C21-C23-H24	120.7	120.7	120.6
C21-C23-C25	118.8	118.8	120.2
H24-C23-C25	119.7	119.7	119.6
C16-C25-C23	121.5	121.5	120.0
C16-C25-H26	120.1	120.1	120.0
C23-C25-H26	119.9	119.9	120.0

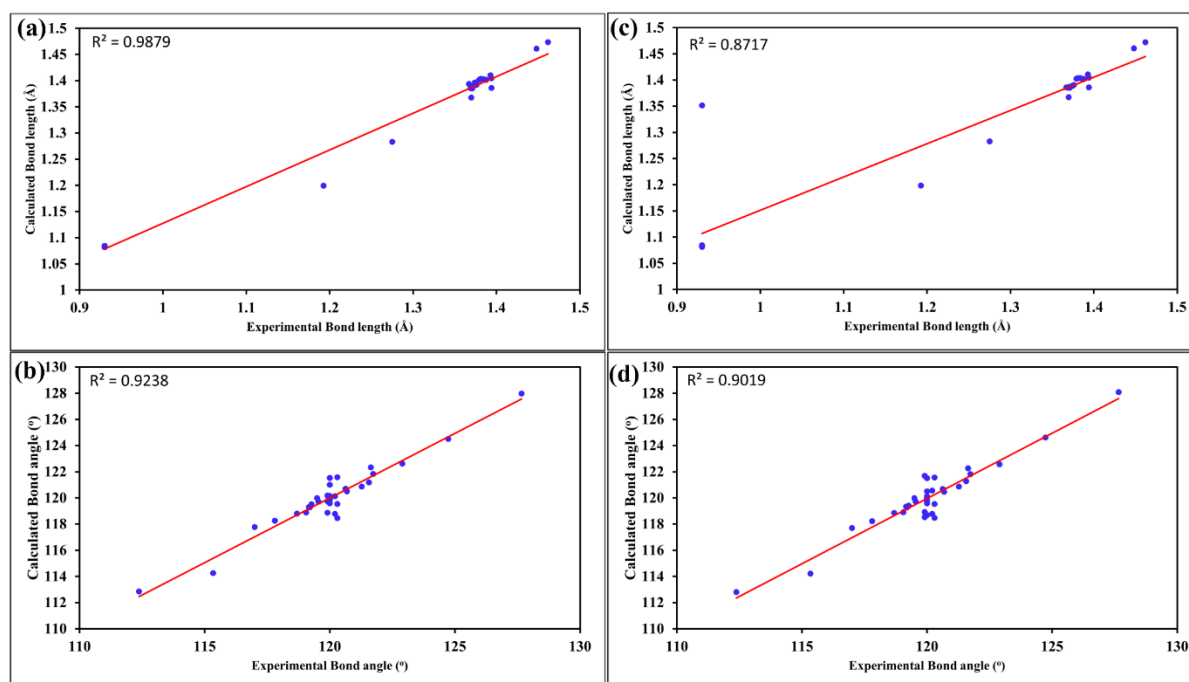


Figure 2. Correlation graphs of the calculated and experimental results: (a) bond distances; (b) bond angles for 2-phenyl-4H-3,1-benzoxazin-4-one; (c) bond distances; (d) bond angles for 2-(4-fluorophenyl)-4H-3,1-benzoxazin-4-one.

3.2. Thermodynamic parameters.

Table 2 lists the thermodynamic properties of the molecules.

Table 2. The thermodynamic parameters of 2-phenyl-4H-3,1-benzoxazin-4-one and 2-(4-fluorophenyl)-4H-3,1-benzoxazin-4-one.

Parameters	DFT-B3LYP/6-311++G(d,p)	
	2PB	2FPB
Optimized global minimum Energy (Hartrees)	-744.328934	-843.597776
Total energy(thermal), E _{total} (Kcal mol ⁻¹)	130.438	125.740
Heat capacity, C _v (cal mol ⁻¹ k ⁻¹)	48.946	51.917
Total Entropy, S (cal mol ⁻¹ k ⁻¹)	110.393	114.630
Translational Entropy (cal mol ⁻¹ k ⁻¹)	42.110	42.341
Rotational Entropy (cal mol ⁻¹ k ⁻¹)	32.695	33.239
Vibrational Entropy (cal mol ⁻¹ k ⁻¹)	35.589	39.050
Vibrational energy, E _{vib} (Kcal mol ⁻¹)	128.660	123.963
Zero-point vibrational energy, (Kcal mol ⁻¹)	122.826	117.597
Rotational constants (GHz)		
A	1.260	1.254
B	0.274	0.204
C	0.225	0.175
Dipole moment (Debye)	2.984	3.212

The dipole moments are extremely high because of the incredibly strong interatomic interactions inside the molecules. Due to the presence of more electronegative nitrogen, oxygen, and fluorine atoms in the molecules, their dipole moments are found to be higher (2.984 and 3.212 Debye). The 2FPB has a greater dipole moment than 2PB because the fluorine atom is attached to the carbon atom. The total energy and entropy of 2PB and 2FPB are determined to be (130.438 and 125.740 Kcal mol⁻¹) and (110.393 and 114.630 cal mol⁻¹ k⁻¹), respectively. The immaterial vibrational energy (zero-point) is achieved for 2PB and 2FPB (122.826 and 117.597 Kcal mol⁻¹). The increased thermodynamic potential of 2PB and 2FPB can be detected by analysing the chemical processes using these thermodynamic properties. All other thermodynamic parameters have also been listed in Table 2.

3.3. Frontier molecular orbitals and DOS spectrum.

The orbitals that possess external electrons are referred to as HOMOs, and they have the ability to contribute their electrons to FMOs. The LUMO is equivalent to the initial excited state that is capable of accepting electrons [21]. The compound's chemical reactivity, hardness, softness, chemical potential, and electrophilic index are all significantly based on the HOMO-LUMO gap (E_{gap}). While a narrow energy gap denotes softness and is associated with strong chemical reactivity and low stability, a big E_{gap} suggests high stability and low chemical reactivity [22]. The oscillator strength, wavelength, excitation energies, and major contributions have all been calculated using the TD-DFT/B3LYP/6-311++G(d,p) technique in order to examine the impacts of the solvent on the electronic structure of the molecules. The results of molecular orbital calculations for 2PB and 2FPB are shown in Table 3. Figure 3 shows the 3D illustration of the border orbitals for the molecules. The whole C-C bond possesses either the benzene ring or the delocalized LUMO of π type. On the other hand, because the HOMO is positioned above the fluorine, oxygen, and nitrogen atoms, the HOMO and LUMO transition implies that the electron density moves from the fluorine, oxygen, and nitrogen atoms to the C-C bonds. For 2PB and 2FPB, the observed HOMO energy is -6.74 and -6.79 eV, respectively. The orbital has the potential to act as an electron donor because of its greater energy value. In contrast, the 2PB and 2FPB, with their respective LUMO energies of -2.26 and -2.33 eV, suggest that they will act as electron acceptors. In 2PB and 2FPB, the energy gap is determined to be 4.48 and 4.46 eV, respectively. Figure 4 displays the projected peak in the UV-visible plot of molecules. For 2PB, the peak is found at 306.1 nm (H \rightarrow L contribution of 76.67%), and for 2FPB, it is seen at 307.1 nm (H \rightarrow L contribution of 75.35%) as given in Table 4. Consequently, the unsaturation of molecules results from the $\pi\rightarrow\pi^*$ type transition caused by the aromatic ring contact. The global reactivity descriptors of molecules have been computed at the DFT level using Koopman's theorem [23]. The findings are displayed in Table 4. The ionization potentials of 6.74 and 6.79 eV and electron affinity values of 2.26 and 2.33 eV have been calculated for 2PB and 2FPB, respectively. These values indicate that the molecules are efficient electron donors and acceptors. A hard molecule has a large energy gap, in contrast to a soft molecule's small energy gap. It has been determined that 2PB has a hardness (η) of 2.24 eV and a softness (S) of 0.22 eV⁻¹, whereas 2FPB has a chemical hardness of 2.23 eV and a softness of 0.22 eV⁻¹. A molecule's reactivity increases when its electronic chemical potential (μ) drops. The chemical potential (μ) values for 2PB and 2FPB are determined to be -4.50 and -4.56 eV, respectively. The opposite of the chemical potential is defined as electronegativity (χ). The enhanced electronegativity (χ) value of 4.50 and 4.56 eV further supports the superior electron acceptor properties of the 2PB and 2FPB molecules.

Using the electrophilicity (ω) scale developed by Domingo et al. [24], organic compounds can be categorized as marginal electrophiles ($\omega < 0.8$ eV), moderate electrophiles ($0.8 < \omega < 1.5$ eV), or strong electrophiles ($\omega > 1.5$ eV). The molecule's electrophilicity indexes (ω) have been found to be 4.52 eV in the 2PB and 4.67 eV in the 2FPB, in contrast to other comparable structures [25]. These results suggest that the molecules are potent electrophiles. It is possible for neighbouring orbitals in a border zone to have the same degenerate energy levels. If so, using HOMO and LUMO alone to characterize border orbitals may not be appropriate. Therefore, using the GaussSum 3.0 tool to combine the molecular orbital data with Gaussian curves, the density of states (DOS) [26,27] was generated. Figure 5 illustrates how a molecule's orbital configuration affects the chemical bonds that atoms form with one another. The density of the state plot is used to show the composition of the system's energy gap. The DOS peaks move as a result of substitutions and changes in the bonding characteristics of the C-C bond inside the rings, which affect the orbitals' energy levels. This reveals the electrical configuration and chemical reactivity of the molecules.

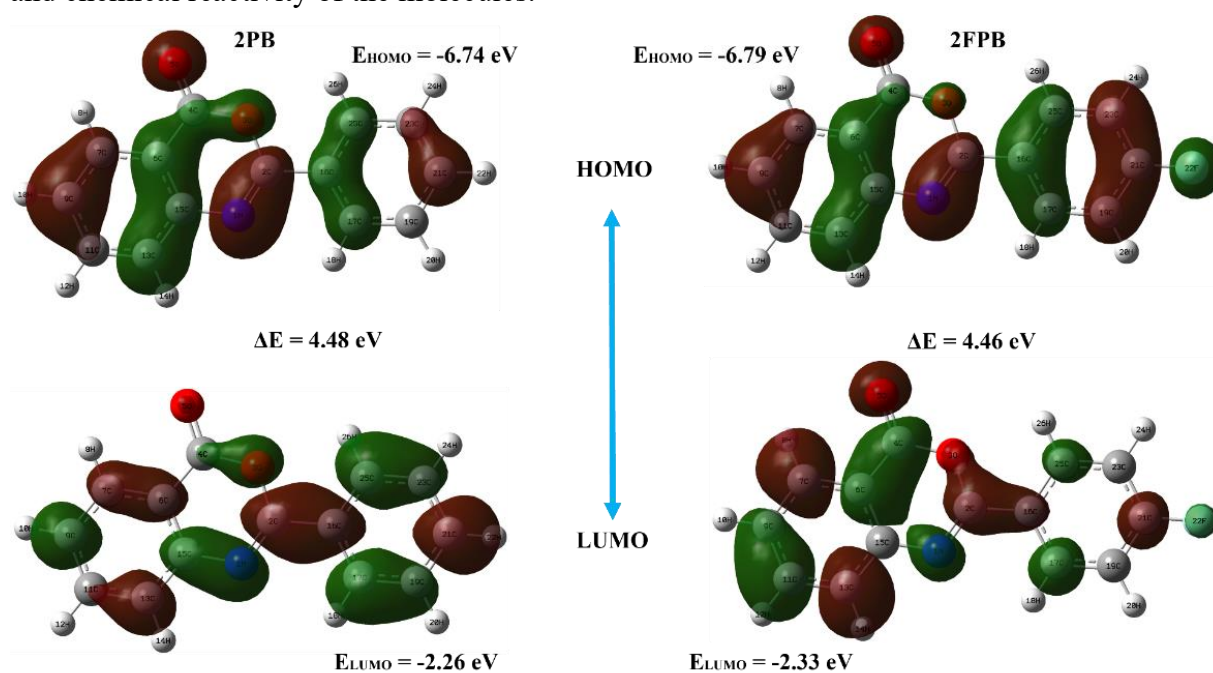


Figure 3. HOMO-LUMO plot for 2-phenyl-4H-3,1-benzoxazin-4-one and 2-(4-fluorophenyl)-4H-3,1-benzoxazin-4-one.

Table 3. Global reactivity descriptors for 2-phenyl-4H-3,1-benzoxazin-4-one and 2-(4-fluorophenyl)-4H-3,1-benzoxazin-4-one.

Molecular Properties	B3LYP/6-311++G(d,p)	
	2PB	2FPB
HOMO (eV)	-6.74	-6.79
LUMO (eV)	-2.26	-2.33
ΔE ($E_{\text{HOMO}} - E_{\text{LUMO}}$) (eV)	4.48	4.46
Ionization potential (I) (eV)	6.74	6.79
Electron affinity (A) (eV)	2.26	2.33
Global hardness (η) (eV)	2.24	2.23
Global softness (S) (eV^{-1})	0.22	0.22
Electronegativity (χ) (eV)	4.50	4.56
Chemical potential (μ) (eV)	-4.50	-4.56
Global electrophilicity (ω) (eV)	4.52	4.67

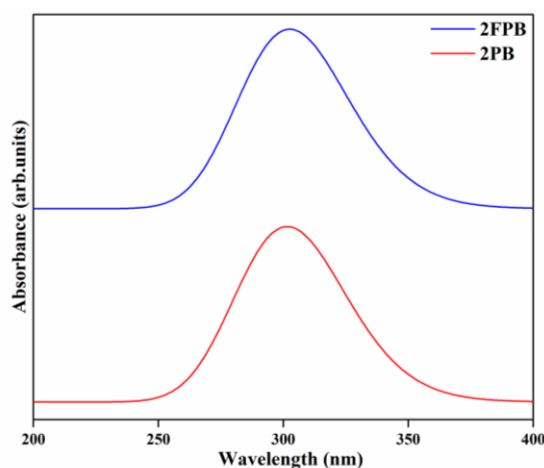


Figure 4. UV-Vis spectra of 2-phenyl-4H-3,1-benzoxazin-4-one and 2-(4-fluorophenyl)-4H-3,1-benzoxazin-4-one.

Table 4. Molecular orbital contributions of 2-phenyl-4H-3,1-benzoxazin-4-one and 2-(4-fluorophenyl)-4H-3,1-benzoxazin-4-one.

TD-DFT/ B3LYP/6-311++G(d,p)				
2PB				
Energy (eV)	Oscillator strength	Computed wavelength (nm)	Major contributions	Assignment
4.051	0.445	306.1	H→L (76.67 %)	$\pi \rightarrow \pi^*$
2FPB				
Energy (eV)	Oscillator strength	Computed wavelength (nm)	Major contributions	Assignment
4.037	0.447	307.1	H→L (75.34%)	$\pi \rightarrow \pi^*$

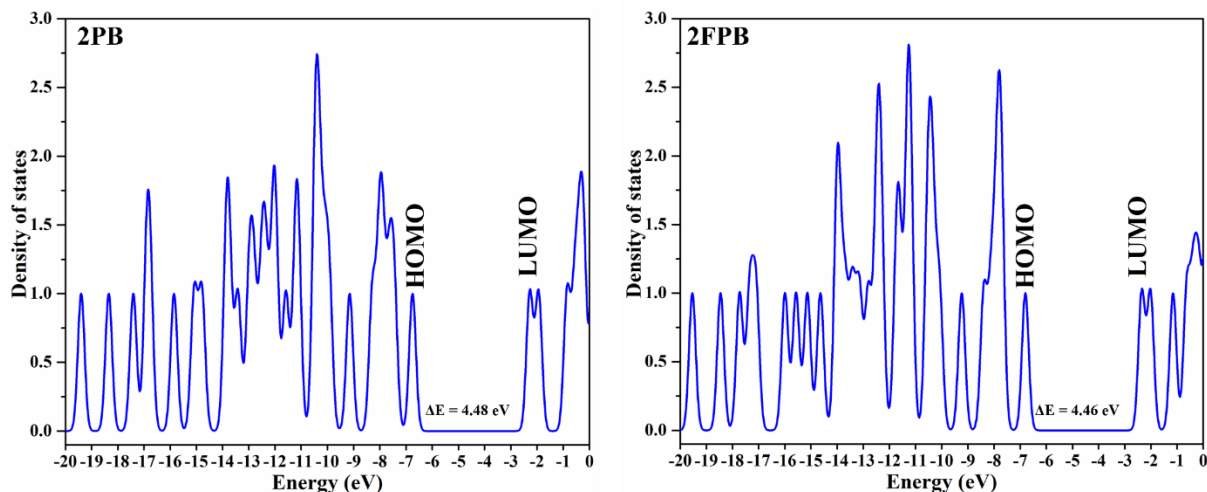


Figure 5. DOS spectrum of 2-phenyl-4H-3,1-benzoxazin-4-one and 2-(4-fluorophenyl)-4H-3,1-benzoxazin-4-one.

3.4. Molecular electrostatic potentials.

By using its various color codes, MEP can assist in illuminating the acceptor regions of a chemical bond reaction. The MEP surfaces of molecules in the gas phase have been calculated in B3LYP/6-311++G(d,p) and are shown in Figure 6 (a) and (b). MEP enhances our understanding of electrophilic reactions, molecular reactivity, and substitution effects by establishing intramolecular interactions with chemically active parts of the molecules. Red, yellow, blue, and green have progressively stronger electrostatic potentials. The lone pair of nitrogen and fluorine atoms in the molecules generates the electron-rich (red) and slightly

electron-rich (yellow) portions. The electron-deficient (blue) portions of the molecules are surrounded by remaining atoms [28]. The potential range of 2PB has been found as $-9.399 \text{ e-}2$ to $9.399 \text{ e-}2$, and for 2FPB, it is calculated as $-9.512 \text{ e-}2$ to $9.512 \text{ e-}2$. The potential range of 2PB is higher than 2FPB because of the attachment of a fluorine atom. The oxygen atom's (O5) electrophilic nature is clearly demonstrated by the red areas that have the highest potential for both molecules. The oxygen (O3) linked to carbon that stands out as the most common is known as nucleophilic patches (blue zone).

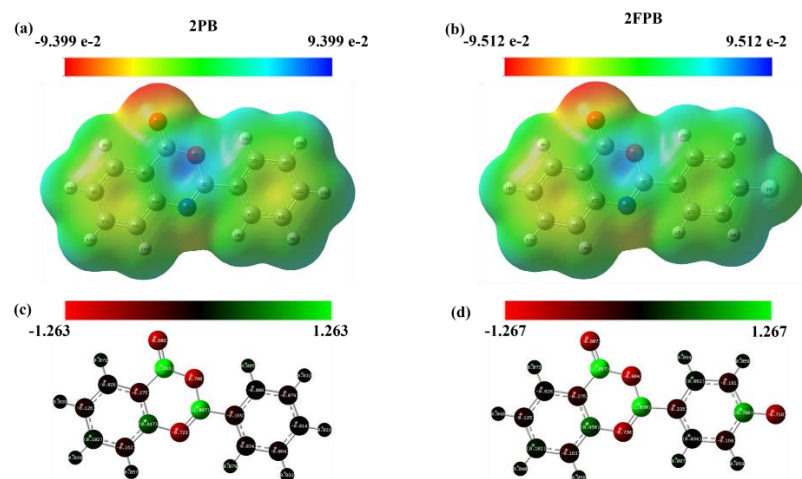


Figure 6. (a), (b) MEP plot for 2-phenyl-4H-3,1-benzoxazin-4-one and 2-(4-fluorophenyl)-4H-3,1-benzoxazin-4-one; (c), (d) Natural population charges for 2-phenyl-4H-3,1-benzoxazin-4-one and 2-(4-fluorophenyl)-4H-3,1-benzoxazin-4-one.

3.5. Natural atomic charge analysis.

The charge distribution throughout a molecule is important in quantum chemistry. Atomic charges are related to a complex's electronic density, charge distribution, and dipole moment [29]. The natural atomic charges (NAC) for 2PB and 2FPB are determined using DFT and are listed in Table 5. The molecules under investigation have atoms of nitrogen, fluorine, and oxygen, which are the most electronegative. The highest electronegative atoms, O3 and O5, bonded to the C4 and C2 atoms are more electropositive when compared to other atoms. The intrinsic atomic charges of the molecules are graphically shown in Figures 6 (c and d). Here, the charge distribution of 2FPB is higher than that of 2PB because the fluorine atom is bonded to the carbon atom C21. Due to the fluorine atom F22 (-0.72) in 2FPB, the two carbon atoms C17 and C25 of the benzene ring are found to be electropositive (0.03 and 0.06). The oxygen atoms O3 and O5 located in the benzoxazine ring have been found to be more electronegative than other natural atomic charges in 2PB (-0.80 and -0.81) and 2FPB (-0.80 and -0.81), as shown in Table 5, respectively. All the hydrogen atoms (H8, H10, H12, H14, H18, H20, H22, H24, and H26) of the molecules are found to be electropositive, and they are predicted to participate in the interatomic hydrogen bonds.

Table 5. Natural population charges and Mulliken atomic charges distribution for 2-phenyl-4H-3,1-benzoxazin-4-one and 2-(4-fluorophenyl)-4H-3,1-benzoxazin-4-one.

Atoms	Atomic charges (natural population) by B3LYP/6-311++G(d,p)		Atomic charges (Mulliken) by B3LYP/6-311++G(d,p)	
	2PB	2FPB	2PB	2FPB
N1	-0.72	-0.73	0.11	0.11
C2	1.01	1.03	-0.34	-0.43
O3	-0.80	-0.80	-0.05	-0.05
C4	1.26	1.27	0.25	0.26

Atoms	Atomic charges (natural population) by B3LYP/6-311++G(d,p)		Atomic charges (Mulliken) by B3LYP/6-311++G(d,p)	
	2PB	2FPB	2PB	2FPB
O5	-0.81	-0.81	-0.29	-0.29
C6	-0.28	-0.28	0.70	0.44
C7	-0.03	-0.03	-0.10	-0.14
H8	0.07	0.07	0.21	0.22
C9	-0.13	-0.13	-0.27	-0.43
H10	0.04	0.04	0.17	0.17
C11	0.10	0.10	-0.37	-0.20
H12	0.04	0.04	0.18	0.18
C13	-0.16	-0.16	-0.17	-0.25
H14	0.06	0.06	0.19	0.19
C15	0.45	0.45	-0.21	0.18
C16	-0.17	-0.24	0.74	0.89
C17	-0.03	0.03	-0.39	-0.57
H18	0.08	0.09	0.19	0.20
C19	-0.06	-0.17	-0.27	0.14
H20	0.03	0.06	0.18	0.21
C21	-0.01	0.78	-0.33	-0.69
H22 (F22)	0.03	-0.72	0.16	-0.16
C23	-0.08	-0.18	-0.33	0.14
H24	0.03	0.06	0.18	0.21
C25	-0.01	0.06	-0.35	-0.54
H26	0.09	0.09	0.21	0.22

3.6. Mulliken atomic charge distribution analysis.

The vibrational characteristics of molecules are significantly connected to the Mulliken charge distribution. Additionally, it provides details on the transfer of charge in reactions [30]. Owing to these characteristics, it also permits the analysis of the dipole moment, polarizability, atom charge distributions, and molecular chemical bond architectures [31]. After examining the many charges of the molecules, it was found that, in the 2PB molecule, the C6 and C16 atoms have the most positive charge relative to the other atoms, while the C2, C11, and C17 atoms have the highest negative charge, as shown in Table 5. Generally, the carbon atoms in the phenyl rings attached to the benzoxazine ring have the highest positive and lowest negative values, according to research reported in the literature [32]. The carbon atom (C16) in the phenyl ring of 2FPB was found to be the most positively charged, whereas the carbon atom (C21) in the benzoxazine ring has the largest negative charge because of F22 bonded to C21. Due to their high electronegativity, the benzoxazine rings of the two compounds were analysed, and it was found that both oxygen atoms had negative charges. In the benzoxazine rings of molecules, every nitrogen atom carried a positive charge due to the surroundings.

3.7. Natural bond orbital (NBO) analysis.

Information on intra- and intermolecular bonding as well as charge transfer is provided by NBO studies [33]. Using the DFT/B3LYP/6-311++G(d,p) basis set, NBO analyses of molecules were carried out using the Gaussian 09 package program. All information gathered has been listed in Table 6 along with the E(2) stabilization energies for 2PB and 2FPB. The transitions from $\sigma(\text{C17-C19})$ to $\sigma^*(\text{C2-O3})$, $\sigma(\text{C17-C19})$ to $\sigma^*(\text{C21-H22})$, and $\sigma(\text{C17-C19})$ to $\sigma^*(\text{N1-C15})$ consist of the maximum stabilization energy for 2PB molecule, which are obtained as 9140.42, 8851.74, and 5108.85 Kcal/mol, respectively. The transitions from $\sigma(\text{C17-C19})$ to $\pi^*(\text{N1-C2})$, $\sigma(\text{C17-C19})$ to $\pi^*(\text{C23-C25})$, and $\sigma(\text{C9-C11})$ to LP(1)C13 are associated with the maximum stabilization energy for 2FPB, which are found as 14.93, 11.88, and 11.66 Kcal/mol,

respectively. These interactions result in high electron densities (about 0.04e, 0.01e, and 0.01e) in 2PB and (approximately 0.16e, 0.19e, and 0.19e) in 2FPB due to the anti-bonding acceptor C-O, C-H, N-C, and C-C orbitals. The strong interaction within LP (1)C13 with the anti-bonding orbitals π (C9-C11) has an energy of 11.66 Kcal/mol in 2FPB, indicating a considerable delocalization. Strong hyperconjugative interactions between carbon and oxygen atoms and the ring structures result in a significant reduction in the lone pair electron density in comparison to other orbitals.

Table 6. Second-order perturbation theory analysis of Fock matrix for 2-phenyl-4H-3,1-benzoxazin-4-one and 2-(4-fluorophenyl)-4H-3,1-benzoxazin-4-one.

Donor(i)	ED (i) (e)		Acceptor (j)	ED (j) (e)		Stabilization energy E(2) (Kcal/mol)	
	2PB	2FPB		2PB	2FPB	2PB	2FPB
π (C6-C7)	0.81	0.81	LP*(1) C15	0.49	0.13	30.52	11.55
π (C6-C7)	0.81	0.81	π^* (C4-O5)	0.13	0.17	11.49	8.84
π (C9-C11)	0.81	0.81	LP (1)C13	0.50	0.19	25.15	11.66
π (C16-C17)	0.81	0.81	π^* (C19-C21)	0.16	0.13	9.15	9.41
σ (C16-C25)	0.98	0.81	σ^* (C7-C9)	0.01	0.19	1464.22	9.42
σ (C17-C19)	0.99	0.99	π^* (N1-C2)	0.13	0.16	1225.12	14.93
σ (C17-C19)	0.99	0.99	σ^* (N1-C15)	0.01	0.16	5108.85	5.99
σ (C17-C19)	0.99	0.82	σ^* (C2-O3)	0.04	0.19	9140.42	11.17
σ (C17-C19)	0.99	0.99	σ^* (C7-C9)	0.01	0.01	735.45	10.64
σ (C17-C19)	0.99	0.99	π^* (C9-C11)	0.17	0.16	677.76	10.96
σ (C17-C19)	0.99	0.84	σ^* (C21-H22)	0.01	0.19	8851.74	8.68
σ (C17-C19)	0.99	0.84	π^* (C23-C25)	0.15	0.19	48.80	11.88
σ (C23-C25)	0.99	0.84	σ^* (C7-C9)	0.01	0.16	1398.49	6.44
π (C23-C25)	0.83	0.99	π^* (C23-C25)	0.15	0.01	17.79	6.00
σ (C25-H26)	0.99	0.99	σ^* (C19-H20)	0.01	0.01	11.53	8.07
σ (C25-H26)	0.99	0.99	π^* (C23-C25)	0.15	0.01	19.48	9.39

3.8. Hirshfeld surface analysis.

One technique for calculating and visualizing intermolecular interactions inside a crystal structure is called Hirshfeld surface analysis. The Hirshfeld surface consists of a specific molecular assembly and a collection of spherical atomic electron solidities. The Hirshfeld surface's exterior and interior partings between the closest atoms are referred to as d_i (density inside) and d_e (density outside), respectively. It is possible to identify the areas that are particularly important for intermolecular interactions using the normalised contact distance (d_{norm}). It is derived from the following equation, which takes into account the atom's Van der Waals (vdW) radii as well as d_e and d_i [34].

$$d_{norm} = \frac{(d_i - r_i^{vdw})}{r_i^{vdw}} + \frac{(d_e - r_e^{vdw})}{r_e^{vdw}} \quad (1)$$

The targeted intermolecular interaction research can benefit from d_{norm} plotting on the Hirshfeld surface, which appropriately highlights the donors and acceptors. The rate of the d_{norm} is positive or negative depending on whether intermolecular contacts are longer or shorter than vdW partings. Crystal Explorer 3.1 was used to perform the Hirshfeld surface computations. The mapped surfaces of the Hirshfeld over d_{norm} (-0.157 to 1.065 a.u.) and (-0.160 to 1.090 a.u.) in 2PB and 2FPB, respectively, are shown in Figures 7 and 8. The surface is depicted as translucent in order to highlight the molecular moiety upon which this computation is based. The Hirshfeld surface is expected to have a volume of 258.21 Å³ in 2PB and 258.91 Å³ in 2FPB, as well as an area of 252 Å² in 2PB and 254.72 Å² in 2FPB. The great separation of the various hydrogen bonding interactions on the d_{norm} front and rear view

surfaces is seen in Figure 7 (a,b) and 8 (a,b). The comparable ranges for the d_e and d_i values, when the Hirshfeld surface is mapped over them, are 1.04 to 2.3 and 2.5 a.u. in 2PB and 1.02 to 2.4 and 2.5 in 2FPB. Figure 7 (c,d) and 8 (c,d) show that shape indices between -1 and 1 a.u., and this value is applicable to curves with curvedness values between -4.0 and 0.4 a.u. [35]. Colour coding is used to depict intermolecular interactions. The dots in red, white, and blue correspond to intermolecular connections with lengths smaller than, equal to, and greater than van der Waals radii, respectively [36]. Hydrogen-bonding interactions are shown by the deep red patches on the d_{norm} surfaces with large circular depressions. Little patches and very light-colored spots on the surfaces, in addition to hydrogen bonds, suggest weaker and longer interactions. The contributions of the intermolecular interactions to the assemblies may be independently measured for each structure and are easily observable on the 2D fingerprint schemes. Figure 7 (g-i) and 8 (g-j) show the deconstructed fingerprint plots, and the contributions coming from different interferences have been examined on the d_{norm} surface. As seen from Figures 7 and 8, the leading C-H hydrogen bonding linkages were represented by two distinct spikes in the 2D fingerprint planes. The C...H/H...C contribution to the Hirshfeld surfaces is most noticeable in the d_{norm} surface. The percentage of C...H/H...C interactions is found to be 17.4% in 2PB and 16.8% in 2FPB from their Hirshfeld surfaces. The C...H connections are represented by a spike with a maximum $d_i + d_e = 6.817 \text{ \AA}$ ($d_i = 3.409 \text{ \AA}$, $d_e = 3.408 \text{ \AA}$) in 2PB and $d_i + d_e = 6.071 \text{ \AA}$ ($d_i = 3.150 \text{ \AA}$, $d_e = 2.921 \text{ \AA}$) in 2FPB, the lowermost and uppermost right portion of the fingerprint plane. This indicates that H-atoms interact with carbon atoms of the phenyl ring and the O5 oxygen atom in 2PB and 2FPB, interacting with the amino hydrogen atom of the phenyl ring, and are responsible for the formation of ring motifs. The inter-contact is estimated to be large since the $d_i + d_e$ value is bigger than the sum of the van der Waals radii of the hydrogen atom (1.09 \AA) and carbon atom (1.7 \AA) [4]. This spike, which appears as enormous red dots on the d_{norm} surface, represents the close associates in the assemblies in Figures 7 and 8.

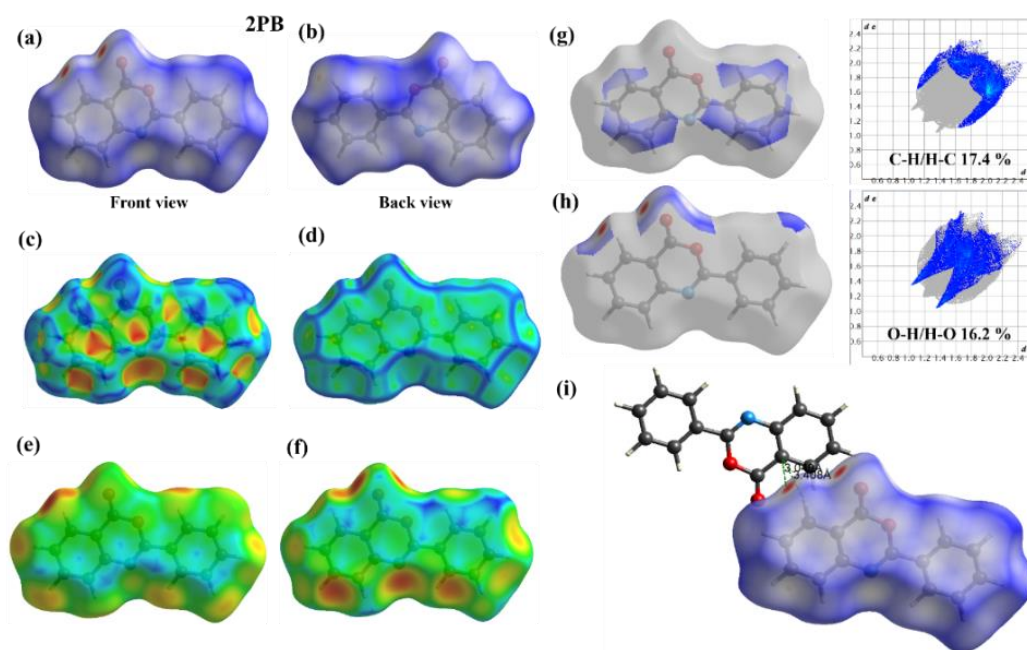


Figure 7. Hirshfeld surfaces mapped over d_{norm} for 2-phenyl-4H-3,1-benzoxazin-4-one (a) front view; (b) back views; (c) shape index; (d) curvedness; (e) density outside d_e ; (f) density inside d_i ; (g and h) 3D and 2D decomposed fingerprint plots; (i) interactions view.

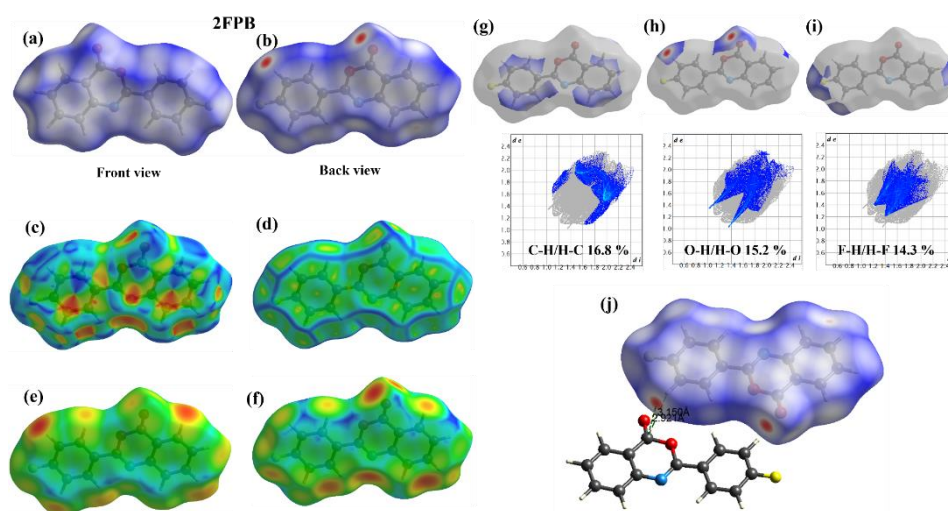


Figure 8. Hirshfeld surfaces mapped over dnorm for 2-(4-fluorophenyl)-4H-3,1-benzoxazin-4-one (a) front view; (b) back views; (c) shape index; (d) curvedness; (e) density outside d_e; (f) density inside d_i; (g, h and i) 3D and 2D decomposed fingerprint plots; (j) interactions view.

The dispersion of scattered points in the fingerprint planes mimics the relative contribution of the O-H interaction, which accounts for 16.2% in 2PB and 15.2% in 2FPB of the total surface portion. The distribution of dispersed points in the fingerprint planes, which accounts for 14.3% of 2FPB, mimics the F-H interaction. Figures 7 and 8 illustrate the diversity of connections that the molecules display, which suggests that the other interactions are minimal (ranging from 1.0 to 4.0 %). Figures 7 and 8 illustrate the interaction between each atom inside the Hirshfeld surfaces and an adjacent atom that is studied. The findings suggested that whole atoms carrying Hirshfeld surfaces should have robust interactions with H atoms close to the surfaces, with the ALL-H interface secretarial for 43.1% and 29.1% of the total interface in 2PB and 2FPB, respectively. These interactions also involve ALL-C, ALL-O, and ALL-N, which have proportional assists of 11.9, 0.8, and 0.3 % in 2PB and 11.5, 0.6, and 0.3 % in 2FPB with inculcated ALL-F. It is important to discuss these interactions because they shed light on the packing of molecules. As seen in Figures 7 and 8, it is computed to determine how one atom inside the Hirshfeld surfaces interacts with each atom closer in order to better study molecular packing. According to the findings of this study, the H atoms in the Hirshfeld surfaces have stronger relationships with the other atoms in the nearby molecules.

3.9. RDG, ELF, and LOL plot analysis.

The Reduced Density Gradient (RDG) has been used to identify strong connections between the structural arrangement and its surroundings, including notable H-bond companions, van der Waals, and repulsive steric forces [37] by non-covalent interactions. Using the Multiwfn 3.4.1 program, the scattered graph and isosurface area were produced [38]. Gnuplot was used to construct the colored scatter plot, and Irfan View 64 was used to display it [39,40]. Strong repulsion (the steric cyclic effect) is represented by the color red, hydrogen bonding interactions are represented by the color blue, and van der Waals interactions are represented by the color green. This investigation yielded the 2D scatter plane and the 3D RDG isosurface solidities of molecules, which are shown in Figure 9 (a,b) and 10 (a,b). The area of these linkages and their graphical depiction are obtained from the RDG research, which is based on the electron density and its by-products. On the graph of $\rho(r)$ against $\text{sign}(\lambda_2)\rho$, the second eigenvalue of the electron density, denoted by $\text{sign}(\lambda_2)\rho$, provides useful information

on the kind and strength of interactions. Repelling, attracting, and van der Waals (VDW) relations are represented by the sign $(\lambda_2)\rho$ values that are, respectively, $\text{sign}(\lambda_2)\rho > 0$, $\text{sign}(\lambda_2)\rho < 0$, and $\text{sign}(\lambda_2)\rho \approx 0$ [41]. Figures 9 and 10 indicate that triple green shade spikes were observed at -0.009, -0.012, -0.0014 a.u. in 2PB and -0.012, -0.0013, -0.0015 a.u. in 2FPB, demonstrating the presence of van der Waals forces in both molecules. On the other hand, small red points have been observed at 0.022, 0.023, 0.03, and 0.04 a.u. in both molecules, indicating the presence of the weak steric force. The presence of non-covalent regions in 2PB and 2FPB molecules is shown by the emergence of blue color spikes. The red flaky areas on the RDG isosurface in the phenyl ring core suggest strong steric activity. Strong hydrogen bonds and blue color patches suggest more attractive and robust bonds, and green flaky patches signify a weak non-covalent interaction.

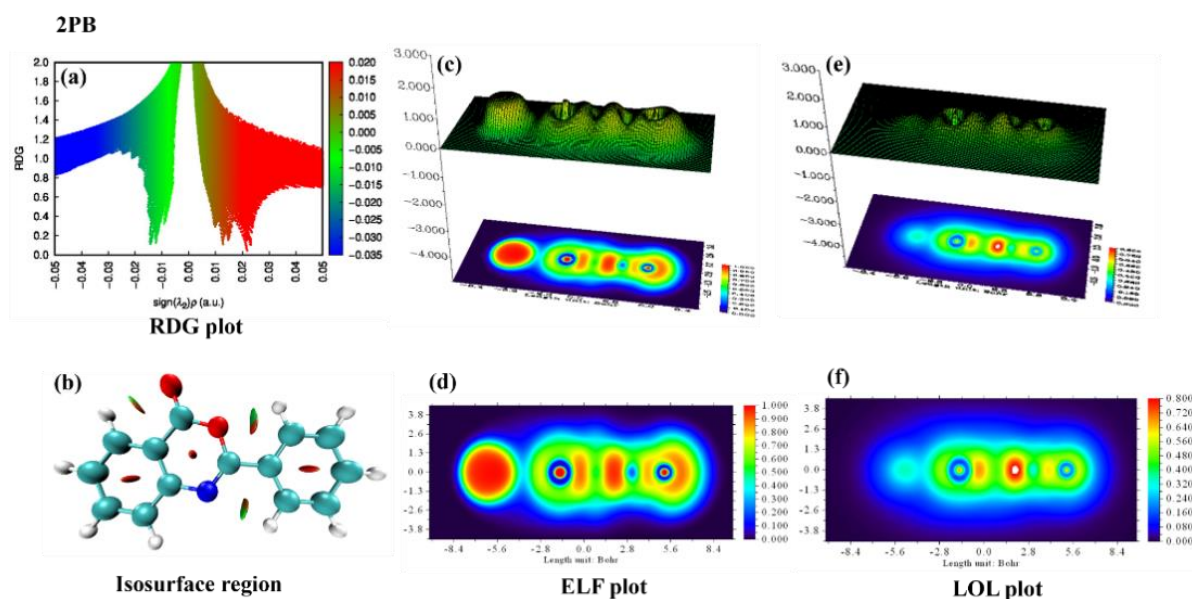


Figure 9. Representation of the outcomes of topological analysis using the Multiwfn program: (a) Scattered RDG plot; (b) Isosurface region; (c) Colour-filled ELF plot; (d) Projected ELF plot; (e) Colour-filled LOL plot; (f) Projected LOL plot of 2-phenyl-4H-3,1-benzoxazin-4-one.

The majority of studies like LOL and ELF just scratch the surface of topological analysis. The likelihood of finding an electron pair on a molecule's surface is highly recommended by the Multiwfn software package. Figures 9 and 10 show the color-shaded plot and relief plot of LOL and ELF, respectively. The large or condensed peak region of the relief chart indicates the electron condition near the corresponding atom. LOL and ELF have parallel chemical configurations as a result of the conditions that depend on kinetic energy density. The electron pair density is explained by ELF, whereas LOL accounts for the maximum localized orbitals overlapping because of the orbital gradient [42,43]. Still, regions with LOL value below 0.5 show delocalized electronic zones, and places where electron localization dominates have LOL greater than 0.5. Regions with ELF values above 0.5 generally correspond to areas of high electron density and strong electron localization [44]. These regions are often associated with covalent bonds or lone pairs of electrons. Figures 9 (c-f) and 10 (c-f) display the advanced ELF and LOL plots, which are in the ranges of 0.0 to 1.0 and 0.0 to 0.8, respectively.

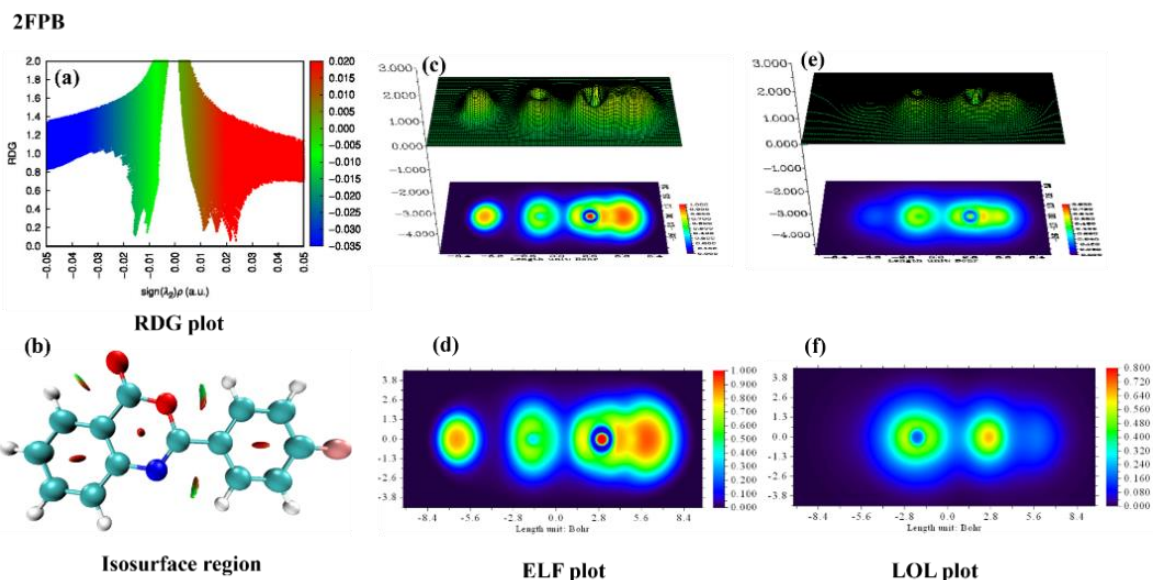


Figure 10. Representation of the outcomes of topological analysis using the Multiwfn program: (a) Scattered RDG plot; (b) Isosurface region; (c) Colour-filled ELF plot; (d) Projected ELF plot; (e) Colour-filled LOL plot; (f) Projected LOL plot of 2-(4-fluorophenyl)-4H-3,1-benzoxazin-4-one.

3.10. In silico molecular docking.

The study of molecular docking is used in pharmacological drug development to examine ligand and protein binding sites [45,46].

Table 7. Molecular docking binding energy of 2-phenyl-4H-3,1-benzoxazin-4-one.

Protein ID	Binding affinity with 2PB (kcal/mol)	H-bonding with distance (Å)	Binding affinity with 2FPB (kcal/mol)	H-bonding with distance (Å)	Binding affinity with Anastrozole (SD) (kcal/mol)
1AQU	-10.4	ARG A: 130 (6.08 Å)	-10.6	ARG A: 130 (6.11 Å) PHE A: 229 (2.70 Å)	-7.1
1M17	-8.4	ASP A: 831 (4.46 Å)	-8.6	ASP A: 831 (4.53 Å)	-8.1

Table 8. Ligand-protein interaction for PDB ID: 1AQU and 1M17 with 2-phenyl-4H-3,1-benzoxazin-4-one and 2-(4-fluorophenyl)-4H-3,1-benzoxazin-4-one.

Protein ID	Amino acid residue of 2PB	Bond type in 2PB	Amino acid residue of 2FPB	Bond type in 2FPB
1AQU	ARG A: 130 GLY A: 259 TRP A: 53 MET A: 232 PHE A: 229	Conventional HB Carbon HB Pi-Pi Stacked Pi-Sulfur Pi-Pi T-shaped	ARG A: 130 GLY A: 259 TRP A: 53 MET A: 232 PHE A: 229 MET A: 256 SER A: 228 THR A: 227	Conventional HB Carbon HB Pi-Pi Stacked Pi-Sulfur Pi-Pi T-shaped Pi-Alkyl Halogen (Fluorine)
1M17	ASP A: 831 ALA A: 719 VAL A: 702 LEU A: 694 LEU A: 820 LYS A: 721 LEU A: 764	Conventional HB Pi-Alkyl Pi-Cation	ASP A: 831 ALA A: 719 VAL A: 702 LEU A: 694 LEU A: 820 LYS A: 721 LEU A: 764 GLY A: 772 MET A: 769	Conventional HB Pi-Alkyl Pi-Cation Carbon HB Halogen (Fluorine)

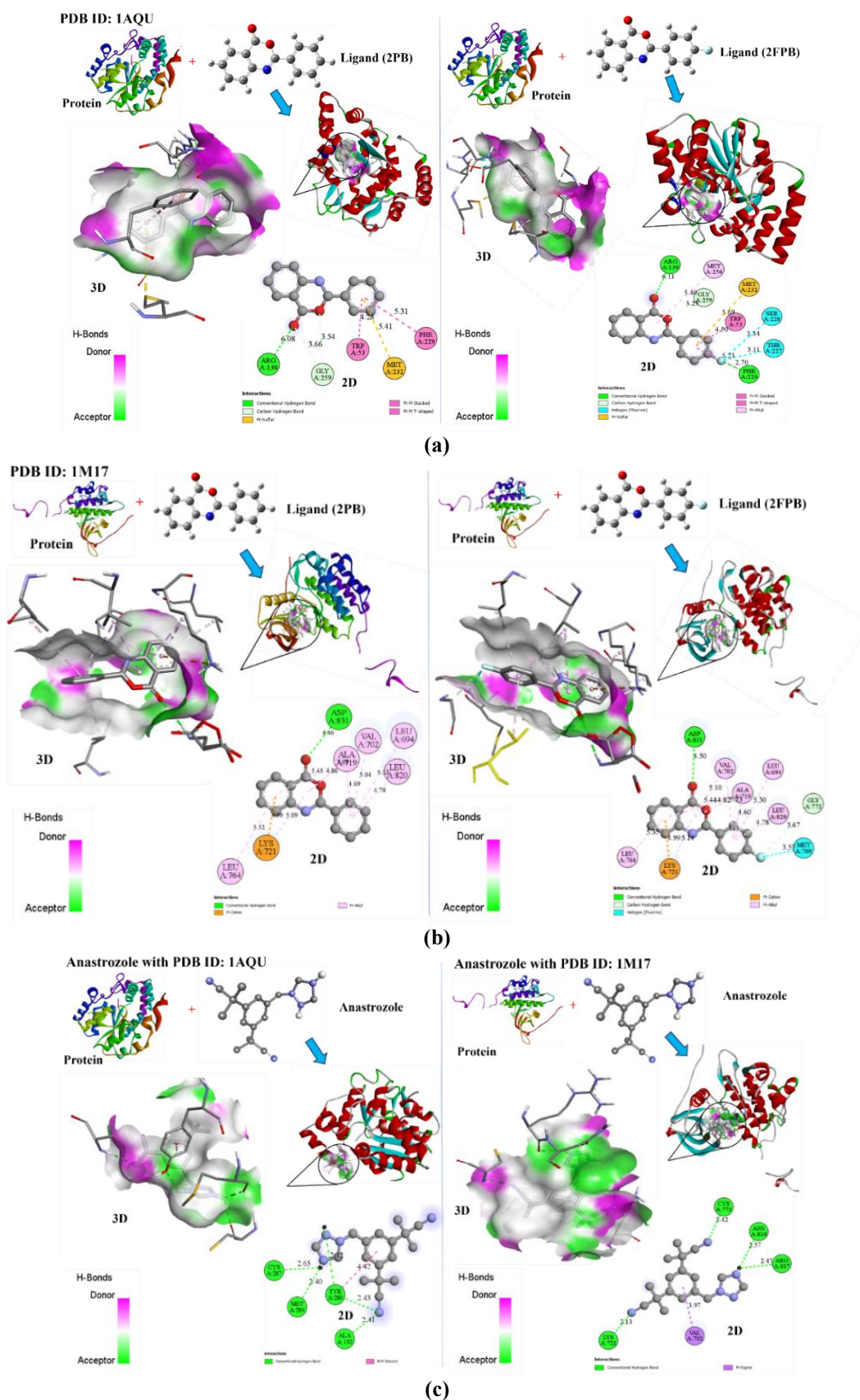


Figure 11 (a) Molecular docking of 3D and 2D interaction with H-Bond donor-acceptor colour grade for 2-phenyl-4H-3,1-benzoxazin-4-one and 2-(4-fluorophenyl)-4H-3,1-benzoxazin-4-one with 1AQU target protein; (b) Molecular docking of 3D and 2D interaction with H-Bond donor-acceptor colour grade for 2-phenyl-4H-3,1-benzoxazin-4-one and 2-(4-fluorophenyl)-4H-3,1-benzoxazin-4-one with 1M17 target protein; (c) Molecular Docking of 3D and 2D interaction with H-Bond donor-acceptor colour grade for anastrozole (standard drug) with 1AQU and 1M17 target proteins.

We have selected breast cancer proteins for docking simulations, including the estrogen sulfotransferase (PDB ID: 1AQU) receptor and the epidermal growth factor (PDB ID: 1M17) receptor, based on previous studies [15]. The standard drug for breast cancer (anastrozole) [16] has been compared with the obtained results. According to docking studies, the molecules showed significant binding affinities with PDB ID: 1AQU (-10.4 Kcal mol⁻¹) and PDB ID: 1M17 (-8.4 Kcal mol⁻¹) in 2PB, and for 2FPB, these are found as -10.6 (1AQU) and -8.6 (1M17) Kcal mol⁻¹. The binding affinities of the standard drug (anastrozole) are found to be -7.1 and -8.1 Kcal mol⁻¹ in 1AQU and 1M17, as shown in Table 7.

Furthermore, the way in which the ligand interacts with the protein explains how the ligand influences the active components of the pathogens that cause illness [47]. Table 8 lists the bond types and residue counts, and Figure 11 (a-c) depicts the 2D schematics for ligand, protein, ligand in protein pocket, hydrogen bonding, and ligand-protein interaction for the molecules in 1AQU and 1M17 [48]. About five contacts in 1AQU and seven distinct interactions in 1M17 have been detected for the ligand-protein interaction through the amino acid residues for the 2PB molecule. MET A: 232 (Pi-Sulfur), PHE A: 229 (Pi-Pi T-shaped), TRP A: 53 (Pi-Pi Stacked), GLY A: 259 (Carbon HB), and ARG A: 130 (Conventional HB) residues interact in 1AQU. Similarly, ALA A: 719, VAL A: 702, LEU A: 694, LEU A: 820, LEU A: 764 (Pi-Alkyl), LYS A: 721 (Pi-Cation), and ASP A: 831 (Conventional HB) residues interact with the 1M17 protein. The ligand 2FPB was also found to have a strong binding affinity in 1AQU, as demonstrated by the two Conventional HB interactions at residues ARG A: 130 (6.11 Å), PHE A: 229 (2.70 Å), one Carbon HB interaction with GLY A: 259, two halogen (Fluorine) interactions at SER A: 228, THR A: 227 residue, and one interaction of the Pi-Sulfur, Pi-Alkyl, and Pi-Pi T-shaped type with residues MET A: 232, MET A: 256 and TRP A: 53, as well as the H-bonding distance (Å) as displayed in Figure 11 (a,b). The residue ASP A: 831 (Conventional HB), five Pi-Alkyl interaction types at LEU A: 764, VAL A: 702, ALA A: 719 and LEU A: 694, GLY A: 772 (Carbon HB), MET A: 769 Halogen (Fluorine), and LYS A: 721 (Pi-Cation) have been depicted in the protein-ligand interaction for the molecule 2FPB with 1M17, as shown in Figure 11 (a,b) and Table 8. It has been determined that the ligand 2FPB has a greater binding affinity (-10.6 Kcal mol⁻¹) toward the 1AQU protein than other proteins based on the outcomes of molecular docking and interaction research, as shown in Figure 12. Hence, the molecule 2FPB may be a more potent inhibitor of the proteins linked to breast cancer.

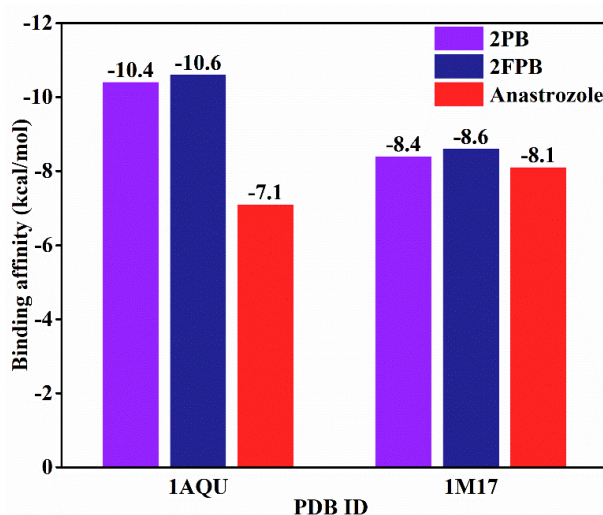


Figure 12. Comparison of the binding energies of 2-phenyl-4H-3,1-benzoxazin-4-one and 2-(4-fluorophenyl)-4H-3,1-benzoxazin-4-one and anastrozole with 1AQU and 1M17 proteins.

3.11. ADMET and Pharmacokinetic prediction.

The results of this investigation, which estimate several pharmacokinetic parameters of the molecule's absorption, distribution, metabolism, excretion, and toxicity, are shown in Table 9. The pkCSM server was utilized in this work. When assessing the drug permeability of drugs taken orally, Caco-2 cells are the most often utilized in vitro model. A higher degree of Caco-2 permeability is indicated if the log Papp value is more than 0.90 (log Papp in 10^{-6} cm/s). The molecules have a log Papp value of 1.388 10^{-6} cm/s, which is considered highly permeable to Caco-2. The human gut is necessary for both food absorption and the absorption of medicinal compounds. Poor intestinal absorption is defined as compounds having an absorption level of less than 30% [19]. Human intestinal absorption rates for 2PB and 2FPB are 98.122 and 96.344 %, respectively. A higher HIA suggests that the drug could be more absorbed when taken orally and passes through the digestive system. Overcoming the protective layer of the skin is the most challenging obstacle in the creation of topical medications. The current medicinal compound's skin penetration level is predicted using a number of in silico techniques. The logKp values of -2.201 and -2.434 in pkCSM server data show that 2PB and 2FPB have superior permeability. The hypothetical volume of distribution, or VDss, is the whole dosage of a drug that would be distributed uniformly to provide a concentration similar to blood plasma. Increased VDss indicates a wider distribution of the medication in tissue compared to plasma. According to the pkCSM prediction model, a high volume of distribution is represented by log VDss >2.81 L/kg. With VDss values -0.154 and -0.234 log VDss, respectively, 2PB and 2FPB have been found, suggesting a sizable volume of dispersion. It appears that the blood-brain barrier (BBB) is a permeable barrier that can shield the brain from dangerous chemicals. A molecule is poorly dispersed to the brain if its logBB is -1, whereas a chemical may readily pass through the blood-brain barrier if its logBB is more than 0.3 [49]. In this study, logBB of 0.536 and 0.537 show that 2PB and 2FPB are extensively dispersed in the brain. Another direct assessment that may be performed with in situ brain insertion and a medication that is instantly injected into the carotid artery is CNS permeability (logPS). According to the pkCSM prediction method, compounds with logPS > -2 are thought to be able to enter the central nervous system (CNS), whereas compounds with logPS < -3 are thought to be unable to do so. The logPS values of 2PB and 2FPB have been found to be -1.356 and -1.337, respectively, suggesting that they have the ability to enter the central nervous system [50]. This work anticipated the inhibitory action of two crucial metabolic components, cytochrome P450 and P-gp. The main enzyme produced in the body for detoxification, cytochrome P450 (CYP), is also involved in the metabolism of medications. The isoforms of cytochrome P450 that are CYP1A2, CYP3A4, CYP2C9, CYP2C19, CYP2D6, and CYP2E1 are known. At dosage concentrations below 10 mM, the cytochrome P450 inhibitor inhibits cytochrome P450 by 50%. Furthermore, the sole enzymes responsible for drug metabolism are CYP2D6 and CYP3A4 [51]. For most cytochrome P450 isoforms, CYP3A4, CYP1A2, and CYP2C19 have effective inhibitory effects in 2PB and 2FPB, whereas other has no such effect. It is believed that the P-gp is present in the hepatic, intestinal, and renal excretory systems. Important phases in the metabolism of drugs include P-gp activation and inhibition. The pharmacokinetic prediction indicates that P-glycoprotein II activity is unaffected by both molecules. 2PB and 2FPB appear to have a renal OCT2 substrate with total clearance rates of 0.921 and 0.782 (log ml/min/kg) according to the pkCSM server [52]. The pharmacokinetic property investigations of molecules meet most of the criteria for drug-likeness and might be regarded as potent cancer

therapeutics. One of the main reasons for drug attrition and a major safety issue for new drug development is drug-induced liver injury. Therefore, according to the PKCSM server, molecules do not cause hepatotoxicity. Human tolerated doses for 2PB and 2FPB were determined to be -0.025 and 0.323 log mg/kg/day, respectively. Oral treatment in rats was computed acute and chronic toxicity limits of 2.002 and 2.143 mol/kg (LD50) and 2.06 and 2.03 log mg/kg bw/day (LOAEL) for 2PB and 2FPB, and they do not suppress hERG I or II [53]. These results were presented in Table 9. Swiss ADME is a free web-based program that assesses the drug similarity, lipophilicity, solubility, and Boiled egg model of the chemicals [54]. The ability of the ligand to cross the Blood-Brain Barrier (BBB) is demonstrated using the BOILED-Egg model. In this study, the yolk component, or yellow region, stands for brain penetration, while the albumin part, or white region, depicts gastrointestinal absorption as shown in Figure 13. The drug ingredient emerges inside the yolk section, indicating the BBB penetrability, according to the BOILED Egg model of molecules created by the Swiss ADME website. The findings show that there is no hydrogen bond donor and that the compounds 2PB and 2FPB only contain three and four hydrogen bond acceptors, respectively. The single exception from the Ghose rule was the molecular weight, which was 223.23 and 241.22 g/mol. The Fraction of sp³ carbon atoms can be used to describe the aliphatic degree and forecast the solubility of medicinal molecules. It has been proposed that the therapeutic success rate of a specific chemical increases with increasing saturation [55]. Fraction Csp³ for the medicinal molecule under research was found to be zero degrees of saturation. Figure 13 displays the radar plot that was acquired. Lipophilicity predictions for iLOGP, XLOGP3, WLOGP, MLOGP, and SILICOS-IT have been found as 2.48, 2.93, 2.86, 2.89, 3.48 for 2PB and 2.54, 3.03, 3.41, 3.29, 3.87 for 2FPB, respectively. The molecules have water solubility ESOL, ALI, and SILICOS-IT and were predicted to be -3.70, -3.50, -5.76 in 2PB and -3.84, -3.60, -6.04 in 2FPB, respectively. The resulting values of water solubility show the variation from moderately soluble to very soluble. These predicted pharmacokinetic properties confirm that the title molecules have not violated most of the parameters and are confirmed to be non-toxic drug candidates.

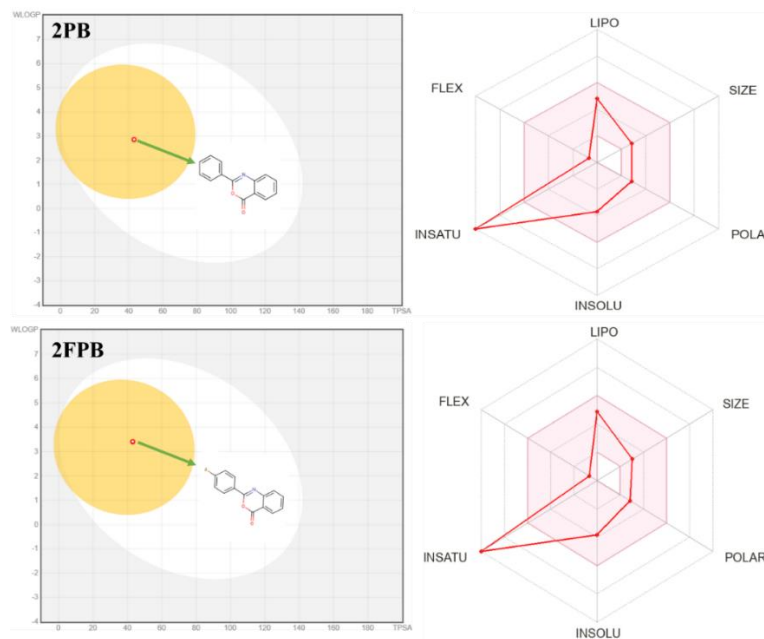


Figure 13. BOILED-Egg plot and Radar plot for 2-phenyl-4H-3,1-benzoxazin-4-one and 2-(4-fluorophenyl)-4H-3,1-benzoxazin-4-one.

Table 9. ADMET profile of 2-phenyl-4H-3,1-benzoxazin-4-one and 2-(4-fluorophenyl)-4H-3,1-benzoxazin-4-one.

ADMET prediction		2PB	2FPB	ADMET prediction		2PB	2FPB	Pharmacokinetic properties		2PB	2FPB
Absorption	CaCo-2 permeability (log Papp in 10 ⁻⁶ cm/s)	1.388	1.388	Excretion	Total Clearance (log ml/min/kg)	0.921	0.782	Physiochemical properties	Molecular weight (g/mol)	223.23	241.22
	Intestinal absorption (human) (%)	98.122	96.344						Number of Hydrogen bond acceptors	3	4
	Skin Permeability (log K _p)	-2.201	-2.434						Number of Hydrogen bond donors	0	0
	P-glycoprotein substrate	No	No						Fraction Csp 3	0.00	0.00
	P-glycoprotein I inhibitor	No	No		Renal OCT2 substrate Renal OCT2substrate	No	No	Water Solubility	ESOL	-3.70	-3.84
	P-glycoprotein II inhibitor	No	No						ALI	-3.50	-3.60
									SILICOS-IT	-5.76	-6.04
Distribution	VD _{ss} (human) (log L/kg)	-0.154	-0.234	Toxicity	AMES toxicity test	Yes	Yes	Lipophilicity	iLOGP	2.48	2.54
	Fraction unbound (human) (Fu)	0.152	0.165		Max. tolerated dose (human) (log mg/kg/day)	-0.025	0.323		XLOGP3	2.93	3.03
	BBB permeability (log BB)	0.536	0.537		hERG I inhibitor	No	No		WLOGP	2.86	3.41
	CNS permeability (log PS)	-1.356	-1.337		hERG II inhibitor	No	No		MLOGP	2.89	3.29
					Oral Rat Acute Toxicity (LD50) (mol/kg)	2.002	2.143		SILICOS-IT	3.48	3.87
Metabolism	CYP2D6 substrate	No	No	Oral Rat Chronic Toxicity (LOAEL) (log mg/kg bw/day)	2.06	2.03	Drug Likeness	Lipinski	Yes	Yes	
	CYP3A4 substrate	Yes	Yes	Hepatotoxicity	No	No		Veber	Yes	Yes	
	CYP1A2 inhibitor	Yes	Yes	Skin Sensitisation	No	No		Ghose	Yes	Yes	
	CYP2C19 inhibitor	Yes	Yes	T.Pyriformis toxicity (log ug/L)	0.807	0.593		Egan	Yes	Yes	
	CYP2C9 inhibitor	No	No	Minnow toxicity (log mM)	0.748	0.392		Bioavailability Score	0.55	0.55	
	CYP2D6 inhibitor	No	No								
	CYP3A4 inhibitor	No	No								

4. Conclusions

In the present work, the molecules 2PB and 2FPB have been studied by DFT. By computing the geometrical parameters using B3LYP/6-311++G(d,p), the optimized structures of the molecules have been ascertained. The TD-DFT algorithm is used to carry out the UV-visible absorption spectra in the gaseous phase. The molecular orbital research states that the kinetic stability, organic reactivity, and intramolecular charge transfer of the molecules influence their bioactivity. Its chemical and biological properties have been identified, along with global reactivity descriptors and DOS spectra. Energy band gap values of 4.48 and 4.46 eV are estimated to be less chemically reactive and more structurally stable for the molecules. The presence of reactive sites is further supported by the molecular electrostatic potential of the molecules. The charge distribution inside each atom of the molecules has been examined using Mulliken and the natural atomic charge population, and the natural bond orbital analysis has been utilised to assess the molecules' intermolecular hydrogen bonding. ELF and LOL studies have been used to evaluate the electronic characteristics of the molecules, and RDG research confirmed their weak contacts. The intensity of atom-to-atom interactions in crystal packing modes is identified using the Hirshfeld surface analysis and 2D finger maps. Molecular docking has been used to evaluate the inhibitory properties against breast cancer proteins. The estrogen sulfotransferase receptor (PDB ID: 1AQU), with which the molecules interact most frequently, is bound with the greatest affinity (-10.4 and -10.6 kcal mol⁻¹). Ultimately, the physicochemical and ADMET properties confirmed the drug-like qualities of the molecules, demonstrating that they are non-toxic and do not break any Lipinski criteria.

Author Contributions

Conceptualization, K.N. and J.S.; methodology, K.N. and J.S.; software, K.N. and J.S.; validation, J.S. and S.S.; formal analysis, K.N. and S.S.; investigation, J.S. and S.S.; resources, K.N. and S.S.; data curation, K.N. and S.S.; writing—original draft preparation, K.N. and S.S.; writing—review and editing, J.S.; visualization, K.N.; supervision, J.S.; project administration, J.S.; funding acquisition, K.N. and S.S.. All authors have read and agreed to the published version of the manuscript.

Institutional Review Board Statement

Not applicable.

Informed Consent Statement

Not applicable.

Data Availability Statement

Data supporting the findings of this study are available upon reasonable request from the corresponding author..

Funding

This research received no external funding.

Acknowledgments

The author would like to thank the management of the Kalasalingam Academy of Research and Education for their encouragement and permission to carry out this research.

Conflicts of Interest

The authors declare no conflict of interest.

References

1. Crafton, S.M.; Venkat, P.S.; Salani, R. A review of the state of cervical cancer: updates from prevention to recurrent disease. *Curr. Opin. Obstet. Gynecol.* **2024**, *36*, 28–33, <https://doi.org/10.1097/GCO.0000000000000918>.
2. Mittelheisser, V.; Gensbittel, V.; Bonati, L.; Li, W.; Tang, L.; Goetz, J.G. Evidence and therapeutic implications of biomechanically regulated immunosurveillance in cancer and other diseases. *Nat. Nanotechnol.* **2024**, *19*, 281–297, <https://doi.org/10.1038/s41565-023-01535-8>.
3. Garcia-Martinez, L.; Zhang, Y.; Nakata, Y.; Chan, H.L.; Morey, L. Epigenetic mechanisms in breast cancer therapy and resistance. *Nat. Commun.* **2021**, *12*, 1786, <https://doi.org/10.1038/s41467-021-22024-3>.
4. Viswanathan, T.M.; Chitradevi, K.; Zochedh, A.; Vijayabhaskar, R.; Sukumaran, S.; Kunjiappan, S.; Kumar, N.S.; Sundar, K.; Babkiewicz, E.; Maszczyk, P.; Kathiresan, T. Guanidine–Curcumin Complex-Loaded Amine-Functionalised Hollow Mesoporous Silica Nanoparticles for Breast Cancer Therapy. *Cancers* **2022**, *14*, 3490, <https://doi.org/10.3390/cancers14143490>.
5. Koca, İ.; Kamaci, V.; Özsoy, C.; Sert, Y.; Kani, İ.; Tutar, L.; Tutar, Y. Pyrazolyl-Benzoxazinone Derivatives as Dual Hsp Inhibitors in Human Breast Cancer. *ChemistrySelect* **2022**, *7*, e202200359, <https://doi.org/10.1002/slct.202200359>.
6. Oyarzo, J.; Bosque, R.; Toro, P.; Silva, C.P.; Arancibia, R.; Font-Bardía, M.; Artigas, V.; Calvis, C.; Messeguer, R.; Klahn, A.H.; López, C. A novel type of organometallic 2-R-2,4-dihydro-1H-3,1-benzoxazine with R = [M(η^5 -C₅H₄)(CO)₃] (M = Re or Mn) units. Experimental and computational studies of the effect of substituent R on ring-chain tautomerism. *Dalton Trans.* **2019**, *48*, 1023–1039, <https://doi.org/10.1039/C8DT03265C>.
7. Ambujakshan, K.R.; Tresavarghese, H.; Mathew, S.; Ganguli, S.; Nanda, A.K.; Panicker, C.Y. Vibrational spectroscopic studies and theoretical calculations of 2-phenyl-4H-3, 1-benzoxazin-4-one. *Orient. J. Chem.* **2008**, *24*, 865–874.
8. Frisch, M.J.; Trucks, G.W.; Schlegel, H.B.; Scuseria, G.E.; Robb, M.A.; Cheeseman, J.R.; Scalmani, G.; Barone, V.; Mennucci, B.; Petersson, G.A.; Nakatsuji, H.; Caricato, M.; Li, X.; Hratchian, H.P.; Izmaylov, A.F.; Bloino, J.; Zheng, G.; Sonnenberg, J.L.; Hada, M.; Ehara, M.; Toyota, K.; Fukuda, R.; Hasegawa, J.; Ishida, M.; Nakajima, T.; Honda, Y.; Kitao, O.; Nakai, H.; Vreven, T.; Montgomery, J.A., Jr.; Peralta, J.E.; Ogliaro, F.; Bearpark, M.J.; Heyd, J.J.; Brothers, E.N.; Kudin, K.N.; Staroverov, V.N.; Kobayashi, R.; Normand, J.; Raghavachari, K.; Rendell, A.P.; Burant, J.C.; Iyengar, S.S.; Tomasi, J.; Cossi, M.; Millam, J.M.; Klene, M.; Knox, J.E.; Cross, J.B.; Bakken, V.; Adamo, C.; Jaramillo, J.; Jaramillo, J.; Gomperts, R.; Stratmann, R.E.; Yazyev, O.; Austin, A.J.; Cammi, R.; Pomelli, C.; Ochterski, J.W.; Martin, R.L.; Morokuma, K.; Zakrzewski, V.G.; Voth, G.A.; Salvador, P.; Dannenberg, J.J.; Dapprich, S.; Daniels, A.D.; Farkas, O.; Foresman, J.B.; Ortiz, J.V.; Cioslowski, J. Fox, D.J. Gaussian 09, Revision d. 01. Gaussian, Inc., Wallingford, **2009**.
9. Preat, J.; Jacquemin, D.; Wathélet, V.; André, J.-M.; Perpète, E.A. TD-DFT Investigation of the UV Spectra of Pyranone Derivatives. *J. Phys. Chem. A*, <https://doi.org/10.1021/jp061260r>.
10. Dennington, R.; Keith, T.; Millam, J. GaussView, Version 5. Semichem Inc., Shawnee Mission, **2009**.
11. O’boyle, N.M.; Tenderholt, A.L.; Langner, K.M. cclib: A library for package-independent computational chemistry algorithms. *J. Comput. Chem.* **2008**, *29*, 839–845, <https://doi.org/10.1002/jcc.20823>.
12. Lu, T.; Chen, F. Multiwfn: A multifunctional wavefunction analyzer. *J. Comput. Chem.* **2012**, *33*, 580–592, <https://doi.org/10.1002/jcc.22885>.
13. Wolff, S.K.; Grimwood, D.J.; McKinnon, J.J.; Jayatilaka, D.; Spackman, M.A. Crystal Explorer 3.0. University of Western Australia, Perth, **2012**.

14. Farzia; Rehman, S.; Ikram, M.; Khan, A.; Khan, R.; Sinnokrot, M.O.; Khan, M.; AlAsmari, A.F.; Alasmari, F.; Alharbi, M. Synthesis, characterization, Hirshfeld surface analysis, antioxidant and selective β -glucuronidase inhibitory studies of transition metal complexes of hydrazide based Schiff base ligand. *Sci. Rep.* **2024**, *14*, 515, <https://doi.org/10.1038/s41598-023-49893-6>.
15. Kunjumol, V.S.; Jeyavijayan, S.; Sumathi, S.; Karthik, N. Spectroscopic, computational, cytotoxicity, and docking studies of 6-bromobenzimidazole as anti-breast cancer agent. *J. Mol. Recognit.* **2024**, *37*, e3074, <https://doi.org/10.1002/jmr.3074>.
16. Karthik, N.; Jeyavijayan, S.; Sumathi, S. Docking studies, molecular structure, and spectroscopic analysis of 3-chlorobenzamide as an anti-cancer agent. *Indian J. Biochem. Biophys.* **2024**, *61*, 204–222, <https://doi.org/10.56042/ijbb.v61i4.8236>.
17. Ounthaisong, U.; Tangyuenyongwatana, P. Cross-docking study of flavonoids against tyrosinase enzymes using PyRx 0.8 virtual screening tool. *Thai J. Pharm. Sci.* **2017**, *41*, 189–192.
18. Dassault Systèmes BIOVIA . Discovery Studio Modeling Environment, Release 2017. Dassault Systèmes; San Diego, CA, USA: **2017**.
19. Pires, D.E.V.; Blundell, T.L.; Ascher, D.B. pkCSM: Predicting Small-Molecule Pharmacokinetic and Toxicity Properties Using Graph-Based Signatures. *J. Med. Chem.* **2015**, *58*, 4066–4072, <https://doi.org/10.1021/acs.jmedchem.5b00104>.
20. Thilagavathy, R.; Kavitha, H.P.; Arulmozhi, R.; Vennila, J.P.; Manivannan, V. 2-Phenyl-4H-3,1-benzoxazin-4-one. *Struct. Rep.* **2009**, *65*, o127, <https://doi.org/10.1107/S1600536808042050>.
21. Albo Hay Allah, M.A.; Balakit, A.A.; Salman, H.I.; Abdulridha, A.A.; Sert, Y. New Heterocyclic Compound as Carbon Steel Corrosion Inhibitor in 1 M H₂SO₄, High Efficiency at Low Concentration: Experimental and Theoretical Studies. *J. Adhes. Sci. Technol.* **2023**, *37*, 525–547, <https://doi.org/10.1080/01694243.2022.2034588>.
22. Jeyavijayan, S. Molecular structure, spectroscopic (FTIR, FT-Raman, ¹³C and ¹H NMR, UV), polarizability and first-order hyperpolarizability, HOMO–LUMO analysis of 2,4-difluoroacetophenone. *Spectrochim. Acta - A: Mol. Biomol. Spectrosc.* **2015**, *136*, 553–566, <https://doi.org/10.1016/j.saa.2014.09.069>.
23. Yossa Kamsi, R.A.; Ejuh, G.W.; Tadjouteu Assatse, Y.; Njeumen, C.A.; Tchoffo, F.; Ndjaka, J.M.B. Computational study of reactivity and solubility of Rubescin D and E molecules in gas phase and in solvent media using Hartree-Fock and DFT methods. *Chin. J. Phys.* **2019**, *60*, 1–11, <https://doi.org/10.1016/j.cjph.2019.04.020>.
24. Domingo, L.R.; Aurell, M.J.; Pérez, P.; Contreras, R. Quantitative characterization of the global electrophilicity power of common diene/dienophile pairs in Diels–Alder reactions. *Tetrahedron* **2002**, *58*, 4417–4423, [https://doi.org/10.1016/S0040-4020\(02\)00410-6](https://doi.org/10.1016/S0040-4020(02)00410-6).
25. Yousif, Q.A.; Fadel, Z.; Abuelela, A.M.; Alosaimi, E.H.; Melhi, S.; Bedair, M.A. Insight into the corrosion mitigation performance of three novel benzimidazole derivatives of amino acids for carbon steel (X56) in 1 M HCl solution. *RSC Adv.* **2023**, *13*, 13094–13119, <https://doi.org/10.1039/D3RA01837G>.
26. Abraham, C.S.; Prasana, J.C.; Muthu, S.; Rizwana B, F.; Raja, M. Quantum computational studies, spectroscopic (FT-IR, FT-Raman and UV–Vis) profiling, natural hybrid orbital and molecular docking analysis on 2,4-Dibromoaniline. *J. Mol. Struct.* **2018**, *1160*, 393–405, <https://doi.org/10.1016/j.molstruc.2018.02.022>.
27. Małęcki, J.G. Synthesis, crystal, molecular and electronic structures of thiocyanate ruthenium complexes with pyridine and its derivatives as ligands. *Polyhedron* **2010**, *29*, 1973–1979, <https://doi.org/10.1016/j.poly.2010.03.015>.
28. Kumar, B.; Devi, J.; Dubey, A.; Tufail, N.; Khurana, D. Thiosemicarbazone ligands based transition metal complexes: A multifaceted investigation of antituberculosis, anti-inflammatory, antibacterial, antifungal activities, and molecular docking, density functional theory, molecular electrostatic potential, absorption, distribution, metabolism, excretion, and toxicity studies. *Appl. Organomet. Chem.* **2024**, *38*, e7345, <https://doi.org/10.1002/aoc.7345>.
29. Halim, S.A.; El-Meligy, A.B.; El-Nahas, A.M.; El-Demerdash, S.H. DFT study, and natural bond orbital (NBO) population analysis of 2-(2-Hydroxyphenyl)-1-azaazulene tautomers and their mercapto analogues. *Sci. Rep.* **2024**, *14*, 219, <https://doi.org/10.1038/s41598-023-50660-w>.
30. Guerrab, W.; Lgaz, H.; Kansiz, S.; Mague, J.T.; Dege, N.; Ansar, M.; Marzouki, R.; Taoufik, J.; Ali, I.H.; Chung, I.-M.; Ramli, Y. Synthesis of a novel phenytoin derivative: Crystal structure, Hirshfeld surface analysis and DFT calculations. *J. Mol. Struct.* **2020**, *1205*, 127630, <https://doi.org/10.1016/j.molstruc.2019.127630>.

31. Govindarajan, M.; Karabacak, M. Spectroscopic properties, NLO, HOMO–LUMO and NBO analysis of 2,5-Lutidine. *Spectrochim. Acta - A: Mol. Biomol. Spectrosc.* **2012**, *96*, 421–435, <https://doi.org/10.1016/j.saa.2012.05.067>.
32. Sevvanthi, S.; Muthu, S.; Raja, M. Quantum mechanical, spectroscopic studies and molecular docking analysis on 5,5-diphenylimidazolidine-2,4-dione. *J. Mol. Struct.* **2017**, *1149*, 487–498, <https://doi.org/10.1016/j.molstruc.2017.08.015>.
33. Ayoob, M.M.; Hawaiz, F.E. Synthesis, crystal structure, DFT calculation and Hirshfeld surface analysis of N-(4-methyl phenyl)-2-(3-nitro-benzamido) benzamide. *Bull. Chem. Soc. Ethiop.* **2024**, *38*, 229–239, <https://dx.doi.org/10.4314/bcse.v38i1.17>.
34. Zochedh, A.; Shunmuganarayanan, A.; Sultan, A.B. Conformational fidelity and hydrogen bond associability of L-histidine with sulfamate anion studied through XRD, quantum chemical, spectroscopic and molecular docking simulation as a cdk-4 inhibitor against retinoblastoma. *J. Mol. Struct.* **2023**, *1274*, 134402, <https://doi.org/10.1016/j.molstruc.2022.134402>.
35. Spackman, P.R.; Turner, M.J.; McKinnon, J.J.; Wolff, S.K.; Grimwood, D.J.; Jayatilaka, D.; Spackman, M.A. CrystalExplorer: a program for Hirshfeld surface analysis, visualization and quantitative analysis of molecular crystals. *J. Appl. Crystallogr.* **2021**, *54*, 1006–1011, <https://doi.org/10.1107/S1600576721002910>.
36. Venkatesan, P.; Thamotharan, S.; Ilangovan, A.; Liang, H.; Sundius, T. Crystal structure, Hirshfeld surfaces and DFT computation of NLO active (2E)-2-(ethoxycarbonyl)-3-[(1-methoxy-1-oxo-3-phenylpropan-2-yl)amino] prop-2-enoic acid. *Spectrochim. Acta - A: Mol. Biomol. Spectrosc.* **2016**, *153*, 625–636, <https://doi.org/10.1016/j.saa.2015.09.002>.
37. Johnson, E.R.; Keinan, S.; Mori-Sánchez, P.; Contreras-García, J.; Cohen, A.J.; Yang, W. Revealing Noncovalent Interactions. *J. Am. Chem. Soc.* **2010**, *132*, 6498–6506, <https://doi.org/10.1021/ja100936w>.
38. Humphrey, W.; Dalke, A.; Schulten, K. VMD: Visual molecular dynamics. *J. Mol. Graph.* **1996**, *14*, 33–38, [https://doi.org/10.1016/0263-7855\(96\)00018-5](https://doi.org/10.1016/0263-7855(96)00018-5).
39. Racine, J. gnuplot 4.0: a portable interactive plotting utility. *J. Appl. Econ.* **2006**, *21*, 133–141, <https://doi.org/10.1002/jae.885>.
40. Noureddine, O.; Issaoui, N.; Medimagh, M.; Al-Dossary, O.; Marouani, H. Quantum chemical studies on molecular structure, AIM, ELF, RDG and antiviral activities of hybrid hydroxychloroquine in the treatment of COVID-19: Molecular docking and DFT calculations. *J. King Saud Univ. Sci.* **2021**, *33*, 101334, <https://doi.org/10.1016/j.jksus.2020.101334>.
41. Saleh, G.; Gatti, C.; Presti, L.L. Non-covalent interaction via the reduced density gradient: Independent atom model vs experimental multipolar electron densities. *Comput. Theor. Chem.* **2012**, *998*, 148–163, <https://doi.org/10.1016/j.comptc.2012.07.014>.
42. Chandran, K.; Zochedh, A.; Sultan, A.B.; Kathiresan, T. Observations into quantum simulation, spectroscopy, electronic properties, pharmacokinetics and molecular docking analysis of lawsone against breast cancer. *J. Mol. Struct.* **2023**, *1293*, 136280, <https://doi.org/10.1016/j.molstruc.2023.136280>.
43. Jumabaev, A.; Koyambo-Konzapa, S.-J.; Hushvaktov, H.; Absanov, A.; Khudaykulov, B.; Holikulov, U.; Ernazarov, Z.; Issaoui, N.; Al-Dossary, O.M.; Nsangou, M. Intermolecular interactions in water and ethanol solution of ethyl acetate: Raman, DFT, MEP, FMO, AIM, NCI-RDG, ELF, and LOL analyses. *J. Mol. Model.* **2024**, *30*, 349, <https://doi.org/10.1007/s00894-024-06147-0>.
44. Jacobsen, H. Localized-orbital locator (LOL) profiles of chemical bonding. *Can. J. Chem.* **2008**, *86*, 695–702, <https://doi.org/10.1139/v08-052>.
45. Rani, K.U.; Sharma, G.V.M.; Saxena, S.; Guruprasad, L.; Padmavathi, D.A. Synthesis, DFT and Molecular docking study of novel bis 1, 2, 3-triazole derivatives of 2-hydroxyquinoline-4-carboxylate as antimicrobial agents. *Indian J. Biochem. Biophys.* **2023**, *60*, 729–740, <https://doi.org/10.56042/ijbb.v60i9.3877>.
46. Kunjumol, V.S.; S., J.; N., K.; and Sumathi, S. Spectroscopic, computational, docking, and cytotoxicity investigations of 5-chloro-2-mercaptobenzimidazole as an anti-breast cancer medication. *Spectrosc. Lett.* **2025**, *58*, 13–35, <https://doi.org/10.1080/00387010.2024.2398025>.
47. Harini, M.; Kavitha, K.; Prabakaran, V.; Krithika, A.; Dinesh, S.; Rajalakshmi, A.; Suresh, G.; Puvanakrishnan, R.; Ramesh, B. Identification of apigenin-4'-glucoside as bacterial DNA gyrase inhibitor by QSAR modeling, molecular docking, DFT, molecular dynamics, and *in vitro* confirmation studies. *J. Mol. Model.* **2024**, *30*, 22, <https://doi.org/10.1007/s00894-023-05813-z>.
48. Kunjumol, V.S.; Jeyavijayan, S.; Karthik, N.; Sumathi, S. Spectroscopic, Computational, Docking and Cytotoxicity Studies on 2-(2-Chlorophenyl)benzimidazole as a Potent Anti-breast Cancer Agent. *Indian J. Pure Appl. Phys.* **2024**, *62*, 576–592, <https://doi.org/10.56042/ijpap.v62i7.7859>.

49. Sukumaran, S.; Azar, Z.; Mohan, V.T.; Bahadur, S.A.; and Kathiresan, T. Theoretical Investigation of 5-Fluorouracil and Tamoxifen Complex – Structural, Spectrum, DFT, ADMET and Docking Simulation. *Polycycl. Aromat. Compd.* **2023**, *43*, 9443-9460, <https://doi.org/10.1080/10406638.2022.2164018>.
50. Belal, A. Drug likeness, targets, molecular docking and ADMET studies for some indolizine derivatives. *Die Pharmazie Int. J. Pharm. Sci.* **2018**, *73*, 635-642, <https://doi.org/10.1691/ph.2018.8061>.
51. Alghamdi, S.S.; Suliman, R.S.; Aljammaz, N.A.; Kahtani, K.M.; Aljatli, D.A.; Albadrani, G.M. Natural Products as Novel Neuroprotective Agents; Computational Predictions of the Molecular Targets, ADME Properties, and Safety Profile. *Plants* **2022**, *11*, 549, <https://doi.org/10.3390/plants11040549>.
52. Muslikh, F.A.; Kurniawati, E.; Ma'arif, B.; Zenmas, S.Z.; Salmasfattah, N.; Dhafin, A.A.; Prasetyawan, F. ADMET Prediction of the Dominant Compound from Mangosteen (*Garcinia mangostana* L.) using pkCSM: A Computational Approach. *Int. J. Contemp. Sci.* **2023**, *1*, 33-38.
53. Han, Y.; Zhang, J.; Hu, C.Q.; Zhang, X.; Ma, B.; Zhang, P. *In silico* ADME and Toxicity Prediction of Ceftazidime and Its Impurities. *Front. Pharmacol.* **2019**, *10*, 434, <https://doi.org/10.3389/fphar.2019.00434>.
54. Azzam, K.A.L. SwissADME and pkCSM Webservers Predictors: an integrated Online Platform for Accurate and Comprehensive Predictions for In SilicoADME/T Properties of Artemisinin and its Derivatives. *Compl. Use Min. Resour.* **2023**, *325*, 14–21, <https://doi.org/10.31643/2023/6445.13>.
55. Kotha Anusha, R.; Mohammed, A.; Sandala Anuradha, b.; Vemuri, J.; Tangeda Saritha, J. Molecular Properties Prediction of Phenothiazine Derivatives by Using Swiss ADME, PkCSM, Lazar and Protox. *World J. Pharm. Sci.* **2019**, *7*, 65-71.

Publisher's Note & Disclaimer

The statements, opinions, and data presented in this publication are solely those of the individual author(s) and contributor(s) and do not necessarily reflect the views of the publisher and/or the editor(s). The publisher and/or the editor(s) disclaim any responsibility for the accuracy, completeness, or reliability of the content. Neither the publisher nor the editor(s) assume any legal liability for any errors, omissions, or consequences arising from the use of the information presented in this publication. Furthermore, the publisher and/or the editor(s) disclaim any liability for any injury, damage, or loss to persons or property that may result from the use of any ideas, methods, instructions, or products mentioned in the content. Readers are encouraged to independently verify any information before relying on it, and the publisher assumes no responsibility for any consequences arising from the use of materials contained in this publication.